

ABSTRACT

Document Title: STREAM-WISE DISCHARGE CHARACTERISTICS OF
 PENDANT SPRINKLER SPRAYS

Chi T. Do, Master of Science, 2009

Directed by: André Marshall, Associate Professor, Department of Fire
 Protection Engineering

Detailed atomization measurements in actual sprinklers are needed for proper spray specification in suppression modeling and analysis. In basic pendant sprinkler configurations, the spray originates from two streams corresponding to flow deflected along the tines of the pendant and flow passing through the void spaces between the tines. In this study, measurements of flow splits (between space and tine streams), sheet breakup distances, drop size, and drop velocity measurements were performed over a range of sprinkler geometries and injection pressures to characterize the near-field sprinkler spray. These detailed measurements were used to support the development of scaling laws describing the effects of injector geometry and injection conditions on sprinkler discharge characteristics.

STREAM-WISE DISCHARGE CHARACTERISTICS OF
PENDANT SPRINKLER SPRAYS

By

Chi T. Do

Thesis submitted to the Faculty of the Graduate School of the
University of Maryland, College Park, in partial fulfillment
of the requirements for the degree of
Master of Science

2009

Advisory Committee:

Professor André W. Marshall, Chair

Professor James G. Quintiere

Professor Peter B. Sunderland

© Copyright by

Chi T. Do

2009

Acknowledgments

This work is supported by the National Science Foundation (NSF) and FM Global. I would like to thank the program managers for their support of the project. I would also like to thank my advisor Dr. André W. Marshall for his guidance and especially his valuable advice that inspires me throughout my years at the Department of Fire Protection Engineering.

I would also like to express my gratitude to the rest of my committee members Dr. James G. Quintiere and Dr. Peter B. Sunderland for their kind support and advice.

I would also like to extend my appreciation to all faculties and staffs of the Department of Fire Protection Engineering at the University of Maryland for passing to me the knowledge in academia as well as in life for the last three years. I also want to thank my fellow student Ning Ren for spending countless hours with me on this project.

I would like to thank my mother for her continuous sacrifices so that I could achieve my goal today. Last but not least, I also want to thank my girlfriend Katarzyna Mazur for her encouragement and support throughout my study. You are my strength and concentration when I needed them the most.

Table of Contents

Acknowledgements	ii
Table of Contents	iii
List of Figures and Tables	iv
Nomenclature	vii
Chapter 1: Introduction.....	1
1.1.Motivation	1
1.2.Literature Review	1
1.3.Research Objectives	8
Chapter 2: Approach	10
2.1.Sprinkler Anatomy.....	12
2.2.Measurements and Diagnostics	14
2.3.Scaling Laws	24
Chapter 3: Results and Discussions	31
3.1.Flow Splits.....	31
3.2.Sheet Breakup Distances	32
3.3.Characteristic Drop Size	40
3.3.1. Horizontal Stream Drop Size	40
3.3.2. Vertical Stream Drop Size	44
Chapter 4: Conclusions.....	47
Appendices	49
Appendix A: Inlet Characterization	49
Appendix B: Spray Images	54
Bibliography	55

List of Figures and Tables

Figures:

Figure 2-1: Sprinkler Atomization Physics	12
Figure 2-2: The Anatomy of Basis and Standard Nozzle	13
Figure 2-3: Inverted PLIF Images Depicting Flow through Sprinkler Spaces	15
Figure 2-4: Flow Split Measurement Setup	16
Figure 2-5: Horizontal Sheet Break-up Distance Measurements	17
Figure 2-6: Vertical Sheet Break-up Distances Measurements and Flow Visualization Apparatus	18
Figure 2-7: Overhead Image for Break-up Distance Determination	19
Figure 2-8: Space Sheet Visualization	21
Figure 2-9: Drop Size and Velocity Measurement Apparatus	22
Figure 2-10: Measurement Locations	24
Figure 2-11: Sheets Geometry	27
Figure 3-1: Observed Trends in Horizontal Sheet Break-up Distances	33
Figure 3-2: Horizontal Sheet Break-up Distances	35
Figure 3-3: Observed Trends in Vertical Sheet Break-up Distances	38

Figure 3-4: Vertical Sheet Break-up Distances	39
Figure 3-5: Observed Trends in Horizontal Stream Characteristic Drop Size	41
Figure 3-6: Horizontal Stream Characteristic Drop Sizes	42
Figure 3-7: Observed Trends in Vertical Stream Characteristic Drop Size	44
Figure 3-8: Vertical Stream Characteristic Drop Sizes	46
Figure A1: Inlet Diagram	49
Figure A2: Pressure Loss Coefficient at Fittings	52
Figure B1: Sheet Break-up Measurements	54

Tables:

Table 2-1: Nozzle Geometries	13
Table 3-1: Flow Split Measurements Results	31
Table 3-2: Measured Horizontal Sheet Break-up Distances	33
Table 3-3: Thickening Factor for Horizontal Sheet	36
Table 3-4: Critical Dimensionless Wave Amplitudes at Break-up for Various Nozzles	36
Table 3-5: Measured Space Sheet Break-up Distances	37
Table 3-6: Flux-based Characteristic Drop Sizes for Horizontal Streams	41

Table 3-7: Flux-based Characteristic Drop Sizes for Vertical Streams	44
Table A1: Inlet Components Geometries	49
Table A2: Flow Tests Results	50
Table A3: Calculated Injection Pressures	53
Table A4: Pressure Losses Percentage at Given Measured Pressure	53

Nomenclature

A	Area, m ²
d	Drop diameter, μm
d_{lig}	Ligament diameter, μm
d_{v50}	Characteristic drop diameter, μm
D_{boss}	Boss diameter, mm
D_d	Deflector diameter, mm
D_{inlet}	Nozzle inlet diameter, mm
D_o	Orifice diameter, mm
D_{pipe}	Inlet section pipe diameter, mm
f	Dimensionless wave amplitude
f_0	Critical sheet break-up dimensionless wave amplitude
g	Gravitational acceleration constant, m/s ²
K	K-factor of sprinkler, lpm/bar ^{1/2}
L_{inlet}	Length of nozzle inlet, mm
L_{jet}	Length of jet before deflector impact, mm
L_{pipe}	Inlet section length, m

m_{lig}	Ligament mass, kg
n	Wave number
$n_{crit,sh}$	Sheet break-up critical wave number
$n_{crit,lig}$	Ligament break-up critical wave number
n_s	Number of spaces of the deflector
n_t	Number of tines of the deflector
Q	Flow rate, m ³ /s
Re	Reynolds Number, UD/ν
r	Radial location, mm
r_d	Deflector radius, mm
$r_{bu,tine}$	Tine sheet break-up location, mm
$r_{bu,space}$	Space sheet break-up location, mm
T	Sheet thickness, mm
T_d	Theoretical sheet thickness at the edge of deflector, mm
U_o	Jet velocity, m/s
U_{sheet}	Sheet velocity, m/s

U_{pipe}	Water velocity inside the pipe, m/s, $4Q/(\pi d_{pipe}^2)$
We	Weber number, $\rho_l U^2 D_o / \sigma$
We_{sheet}	Sheet Weber number, $\rho_l U_{sheet}^2 D_o / \sigma$
X_{sheet}	Sheet break-up scaling parameter
X_{drop}	Drop size scaling parameter

Greek letters

β	Thickening factor, U_o / U_{sheet}
ε	Pipe roughness factor
σ	Surface tension, N/m
γ	Flow split factor
λ	Wavelength
θ_{boss}	Angle of deflector boss
θ_{space}	Angle of deflector space
θ_{tine}	Angle of deflector tine
ρ	Density, kg/m ³
μ	Dynamic viscosity, kg/ms

ν Kinetic viscosity, m²/s

Subscripts

a Air

l Liquid (water)

s Space

t Time

Chapter 1: Introduction

1.1. Motivation

Although several experimental and analytical research efforts have been conducted to better understand discharge characteristics from fire suppression devices [1], the atomization process in sprinkler sprays and its relationship with geometry still remains enigmatic. This gap in knowledge prevents the development of physical models to predict and describe the initial sprinkler spray.

In this study, a series of experiments were conducted to support sprinkler atomization model development and to contribute to the limited database of fire sprinkler measurements. These experiments employ a range of sprinkler configurations (from simple laboratory geometries to actual commercial nozzles) with a focus on characterizing stream-wise breakup processes to provide insight into the relationship between injection conditions and the initial sprinkler spray.

1.2. Literature Review

Despite diversity in size, shape, and design details, most modern fire sprinklers use the same fundamental method of spray generation. Water is initially forced through an orifice to produce a continuous water jet. This jet then impinges onto a deflector to form a thin sheet of water. The sheet subsequently disintegrates into ring-like ligaments and ultimately into drops. Having this picture in mind, the sprinkler atomization process can

be divided into stages for focused measurements and analysis. Several fundamental atomization studies have developed theories to describe physical processes relevant to fire sprinkler spray generation. There is also a separate body of more applied research focused on quantifying discharge characteristics (i.e. drop size and velocity) and dispersion behavior from fire sprinklers. In the following sections, these studies will be summarized and discussed to provide some background and to present the current understanding of sprinkler atomization physics.

Numerous fundamental studies have been conducted to examine the atomization process responsible for transforming continuous liquid streams into discrete drops. These studies considered the fundamental physical processes leading to atomization and their dependence on injection and environmental conditions. A few atomization studies relevant to sprinklers are presented in the following.

Dombrowski and Hooper developed mathematical equations to describe sinuous break-up and dilatational break-up modes [2]. They also extended these equations to predict wavelength and drop sizes in each break-up mode. These analytical results compared favorably to their experimental data, obtained by using high speed flash (i.e., short exposure time) photography on water sprays generated by a fan-spray nozzle in a pressure vessel. Since these break-up modes have been observed in sprinkler atomization for a wide range of operating conditions, Dombrowski and Hooper's analysis provides insight for sprinkler sprays, despite nozzle configuration differences.

Huang utilized a high-speed motion (6000 frames per second) photographic technique to study the break-up mechanisms of liquid sheets, formed by the impingement of two co-axial jets [3]. He reported three break-up regimes and their trends by plotting the ratios of break-up radii over nozzle radius against the jet Weber number, $We = \rho U^2 D / \sigma$. In the first break-up regime, occurring when the Weber number falls in the range from 100 to 500, droplets are formed through successive detachment of liquid beads along the nearly circular periphery of the sheet. The sheet break-up distance in this regime can be described by $2r_{bu,sh} / D_o = 0.167We$. The second regime occurs when the Weber number is in the range from 500 to 2000. In the first half of this regime, a cardioid wave pattern appeared on the sheet whereas in the second half, sinuous motion was observed. The last regime occurs when the Weber number is in the range from 2000 to 30000. The disturbance on the sheet dramatically increases. Ring-like ligaments appear in this regime, and drops are formed when these ligaments disintegrate. The sheet break-up distance was shown to follow the semi-empirical equation $2r_{bu,sh} / D_o = 1250We^{-1/3}$.

Prahl and Wendt explored the break-up locations of liquid sheets, generated by impinging a jet onto a flat disk using a high-speed photographic technique [4]. The objective of this study was to find the critical wavelength at which break-up occurs. Prahl and Wendt introduced controlled disturbances (amplitude and frequency) into the sheets by varying the vibration of the deflector disk. Subsequently, by determining the vibrating frequency, which caused the earliest break-up at a given operating condition, the critical wavelength could be found. Their results also showed that the break-up locations follow

the $We^{-1/3}$ scaling, proposed by Huang. Besides break-up mechanism, Prah1 and Wendt also developed a model for drop trajectory, assuming quiescent air and flow trajectory angle distribution, capable of predicting their experimental results.

More recently, Clanet and Villermaux conducted a series of experiments to study the formation and disintegration of smooth and flapping liquid sheets, generated by impinging a jet onto a flat deflector [5, 6]. They found break-up distance trends similar to those reported by Huang despite differences in experimental configuration. The arithmetic drop diameter was also examined. Clanet and Villermaux found that this mean diameter can be described by $d / D_o = (\rho_a / \rho_l)^{-2/3} We^{-1}$ for Weber number in the range from 1000 to 2000.

A number of experiments have been conducted over the past four decades to measure the discharge characteristics of sprinkler sprays. These experiments utilized a wide range of experimental methods and diagnostics, including simple short exposure photography and more advanced diagnostic techniques such as Phase Doppler Interferometer (PDI) and Particle Image Velocimetry (PIV).

Dundas evaluated scaling laws proposed by Heskestad, $d_{v50} / D_o = NWe^{-1/3}$ where d_{v50} is the volumetric median diameter, D_o is the nozzle diameter, and N is a constant ranging from 1.74 to 3.21 [7]. He conducted a series of measurements with six geometrically similar sprinklers whose orifice diameters varied from 3.1 to 25.4 mm under a wide range of operating pressures, from 0.345 to 5.25 bar. He employed a high-speed photographic technique to capture 18 still images for each condition, and then

counted and measured drop size manually or with an electronic scanner. His results showed that the ratio of volumetric median diameter to nozzle orifice diameter followed Heskestad's correlation using the constant of 1.413. He noted that this number was below the wide range of values previously reported for a variety of nozzle configurations.

More than a decade later, Yu employed a laser-based imaging technique to measure drop size from three upright sprinklers with orifice diameter of 12.7 mm, 13.5 mm, and 16.3 mm [8]. His measurements were taken at two different elevations (3 m and 6 m) below the sprinkler heads. The overall characteristic drop size measured at these two elevations were almost identical and followed a $We^{-1/3}$ scaling law consistent with Dundas's sprinkler measurements.

The Phase Doppler Interferometry (PDI) technique was first validated and utilized by Widmann to measure the spray from four real sprinklers with orifice diameters of 8.0 to 11.0 mm, operated at 0.69 to 2.0 bar [9, 10]. This technique provides detailed local measurements of drop size and drop velocity by monitoring the fluctuation in intensity of scattered light from two laser beams when particles pass through their intersection. Although this technique provides highly accurate data, it is limited to a small sample volume where the two lasers intersect. Because of the limitations of the PDI technique, Widmann was only able to analyze local measurement trends. He showed that the local mean volume drop diameter d_{30} followed a $We^{-1/3}$ scaling law for a range of pressures from 0.93 to 2.0 bar. At low pressure (0.69 bar), the local mean volume drop size was smaller than that predicted by the scaling law.

Soon after Widmann, Sheppard made his contribution to the database of sprinkler spray measurements through a comprehensive set of experiments on 16 commercially available pendant and upright sprinklers whose orifice diameters ranged from 9.5 to 25.4 mm with operating pressures ranging from 0.345 to 5.52 bar [11, 12]. The drop trajectories and terminal velocities were calculated assuming spherical drops to develop a correlation of the volume median drop diameter as a function of horizontal distance. Sheppard reported that the correlation compared favorably to his experimental results. Employing PDI techniques, Sheppard also obtained local measurements of drop size at various azimuthal and elevation angles. Sheppard also applied the PIV technique to measure drop velocity. The velocity magnitude data, presented in spherical coordinates with the sprinkler head at the center, showed significant variation with elevation angle. Using his velocity data, Sheppard showed that at location near the sprinkler, i.e. ~ 0.2 m, drop velocity is about 53% of jet velocity at the orifice and can be approximately expressed as $U = 0.6(P/\rho_l)^{-1/2}$. Moreover, at these locations, drop velocity appeared to be purely radial with the virtual origin located between the orifice and deflector for pendant sprinklers and between the orifice and slightly above the deflector for upright sprinklers.

Putorti measured drop size and velocity simultaneously using Particle Tracking Velocimetry and Imaging (PTVI) technique [13]. The nozzles with diameters ranging from 4.07 mm to 8.48 mm were operated at pressures between 0.21 and 4.34 bar. The water jet in these nozzles was injected onto fabricated conical deflectors, with angles of 60° , 90° , and 120° . Drop sizes from 0.2 mm to 3.0 mm, and velocities from 1 m/s to 30

m/s were reported. The volumetric median drop size found in Putorti's study appeared to follow a $We^{-2/3}$ scaling law. While calculating drop trajectory, Putorti assumed that the droplets started at the sprinkler with a velocity equal to the jet velocity at the nozzle. This drop trajectory was then utilized to obtain the theoretical mass flux distribution on the floor and compared satisfactorily to his measurements. Thus, he further suggested that sheet break-up region and mechanism can be neglected for trajectory analysis.

Most recently, sprinkler measurements were conducted by Blum [14] and Ren [16 - 18]. They explored the impacts of sprinkler components by using three different types of nozzle configurations. In the simplest configuration, the Basis Nozzle, a jet was orthogonally injected onto a flat circular deflector disk having a diameter of 38 mm. Jet were created with orifices having diameters ranging from 3.5 to 9.7 mm. The Tined Nozzle, was constructed by modifying a commercially available Tyco D3 nozzle where the boss, the central conical component on the deflector, was removed A commercially available Tyco D3 spray nozzle with an orifice diameter of 6.35 mm, referred to as the Standard Nozzle, was used for the third and final nozzle configuration. Blum utilized high-speed flash photography and Planar Laser Induced Fluorescence (PLIF) techniques to measure sheet trajectory angles and sheet break-up distances. He found that break-up distances produced by the Basis, Tined, and Standard Nozzles all follow a $We^{-1/3}$ scaling law. He also pointed out that the boss in the Standard Nozzle increased sheet instability resulting in significantly shorter breakup distances. Moreover, employing a Spraytec Particle Analyzer by Malvern Instruments, Blum also measured the local drop size 1 m below the nozzles at operating pressures of 0.69 to 2.76 bar. He found that for the Basis

and Tined nozzles, the characteristic drop sizes did not change significantly with respect to Weber number whereas the Standard nozzles produced drops that followed a $We^{-1/3}$ scaling law. These results are consistent with those found in similar configurations by Clanet, Villermaux, and Dundas. Based on Blum's local drop size and mass flux data, Ren estimated the overall characteristic drop sizes for the three nozzle configurations. He analyzed how drop size depends on the nozzle configuration. Using short exposure photographic technique, Ren also presented two different break-up modes, i.e. rim break-up and ligament break-up mode. Rim break-up mode, occurring when $We_{sheet} < 150$, was described as drops detachment at the edge of the sheet. On the other hand, ligament break-up mode, occurring at $We_{sheet} > 150$, consists of the transformations from sheet to ligaments and from ligaments to drops.

1.3. Research Objectives

Previous sprinkler spray studies have provided a wide range of sprinkler discharge measurements with limited discussion on how the spray is generated and with limited explanations concerning the observed behavior. As a result, the effect of sprinkler geometry on the atomization process is not fully understood. In this study, the relationship between the sprinkler geometry and spray characteristics is explored through a series of systematic measurements, carefully performed along the two distinct streams originating from the tines and void spaces between the tines of a pendant sprinkler. These measurements quantify the flow split between the tine and space streams and their

respective sheet break-up characteristics, which govern critical initial spray quantities like drop velocity and drop size, also measured in this study.

In addition to these measurements, this study also reveals the spray topology through visualization of the radially expanding sheets created along the deflector and the orthogonal fan sheets created from the flow forced through the void spaces between the tines. This visualization provides insight into the break-up mechanisms responsible for the initial spray. The combination of flow visualization and detailed stream-wise measurements conducted in this study provides valuable information for the development of a physics based sprinkler atomization model (SAM) in which sprinkler discharge characteristics can be determined from sprinkler geometry and operating conditions [16, 19].

Chapter 2: Approach

Drop size and drop velocity are generally considered the most important quantities for evaluating the sprinkler spray. These quantities are typically measured and reported to characterize the spray for a particular sprinkler configuration. In order to design sprinklers and analyze their performance, it is of interest to understand how sprinkler geometry and injection conditions affect the initial spray. However, typical drop size and drop velocity measurements do not provide insight into the atomization process that governs these initial spray quantities. Therefore, intermediate measurements are needed to establish the relationship between injection details and discharge characteristics such as drop size and velocity. In this study, a series of measurements were conducted to evaluate the transformational stages of the atomization process for two geometrically different classes of nozzles over a range of operating pressures.

Essential features of the atomization process relevant to fire sprinklers are captured in the impinging jet configuration shown in Figure 2-1 where a liquid jet is orthogonally injected onto a flat disk. After impact, the jet is transformed into a thin film, moving radially outwards on the deflector surface. This film formation is the first stage of the atomization process in sprinklers. A useful model for predicting the film thickness and velocity along the deflector based on a free-surface similarity boundary layer concept was developed by Watson [20] and adapted for sprinkler analysis by Di [16]. This boundary layer model is also used for analysis in this study.

The film is transformed into an unconfined sheet as it expands beyond the deflector edge. This sheet is inherently unstable due to growing sinuous waves, formed on the sheet. As the sheet travels radially outwards, the wave amplitude continues to grow because of pressure difference between the sheet upper and lower surfaces. At a critical wave amplitude, the sheet breaks up into ring-like fragments, called ligaments completing the second stage of the atomization process (i.e., sheet to ligament transformation).

The ligaments are also unstable by nature. As they expand outwards, aerodynamic forces cause dilatational waves to grow along the ligament. When these dilatational waves reach their critical amplitude, the ligaments break into smaller fragments. Due to surface tension, these fragments contract to form drops completing the final stage of the atomization process (i.e. ligament to drop transformation). More detailed discussions of the sprinkler atomization process and associated mathematical models can be found in Wu [14, 15] and Ren [17].

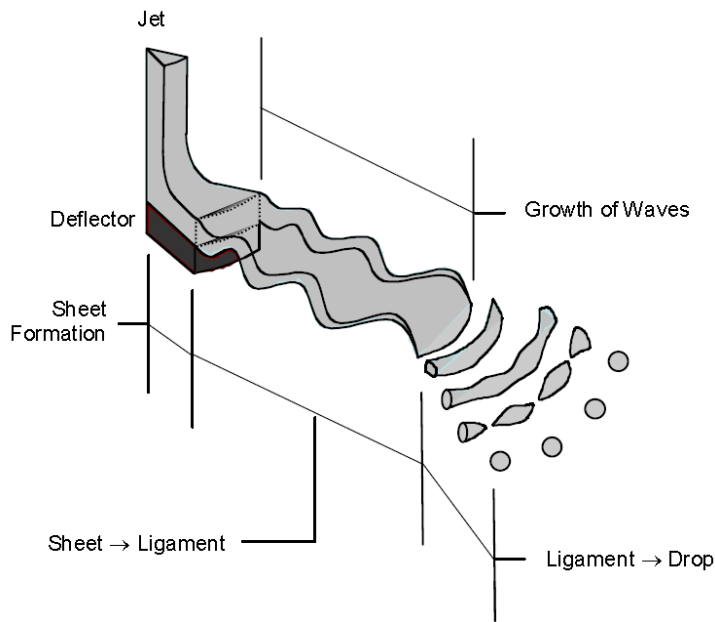


Figure 2-1: Sprinkler Atomization Physics [15]

2.1. Sprinkler Anatomy

In this study, two different types of nozzles were employed as illustrated in Figure 2-2 and summarized in Table 2-1. The Basis Nozzles were used to study the fundamental impinging jet atomization, where a jet impinges orthogonally onto a flat circular disk. In this configuration, the complexities of boss, tines, and space typical of actual sprinklers are removed. Using the measured Basis Nozzle atomization behavior as a baseline, the effects of more complex geometric features (i.e. boss, tines, and spaces) were introduced in the Standard Nozzle configuration (commercially available Tyco D3 nozzles) to explore how more realistic geometric features affect spray behavior.

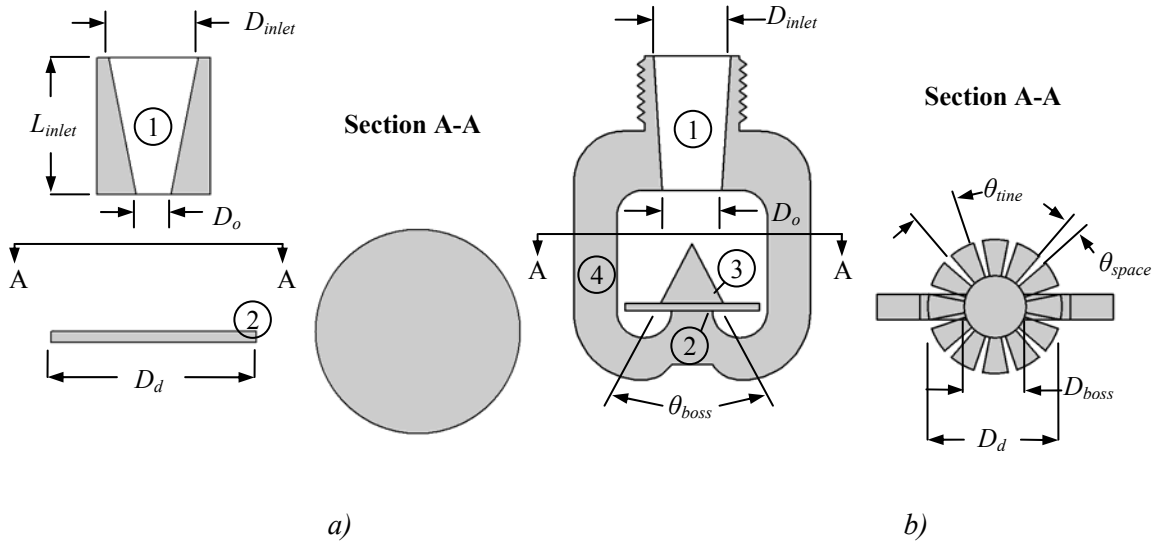


Figure 2-2: The Anatomy of Basis and Standard Nozzle: a) Basis Nozzle, b) Standard Nozzle

1: Inlet, 2: Deflector, 3: Boss, 4: Frame Arms

Table 2-1: Nozzle Geometries

		Basis Nozzles			Standard Nozzles	
		Small	Medium	Large	Medium	Large
Inlet Characteristics	D_{inlet} (mm)	16.5			10.1	14.6
	L_{inlet} (mm)	25.4			25.4	
	L_{jet} (mm)	25.4			21.2	
	D_o (mm)	3.2	6.4	9.5	6.4	11.3
	K-Factor (lpm/bar ^{1/2})	7.2	25.9	49.0	25.9	80.7
Deflector Characteristics	D_{def} (mm)	38.0			25.4	
	θ_{tine} (°)	N/A			22	
	θ_{space} (°)				8	
Boss Characteristics	D_{boss} (mm)	N/A			11.9	
	θ_{boss} (°)				56	

A well characterized 0.47 m inlet section downstream of the flow pressure measurement station was used to provide a ‘clean’ consistent upstream boundary condition for the nozzles used in this study. A description of the inlet loss characterization approach needed for determining nozzle injection pressures is provided in Appendix A.

2.2. Measurements and Diagnostics

Through flow visualization, Blum observed that idealized pendant sprinkler sprays typically consist of two distinct streams, i.e., the horizontal streams formed along the tines and the vertical streams produced by forcing water through the void spaces between them [14]. In this study, these two streams, shown in Figure 2-3, were characterized through a series of stream-wise measurements quantifying the flow split (between the tines and spaces), sheet break-up distances, drop sizes, velocities and their relationship with injection conditions.

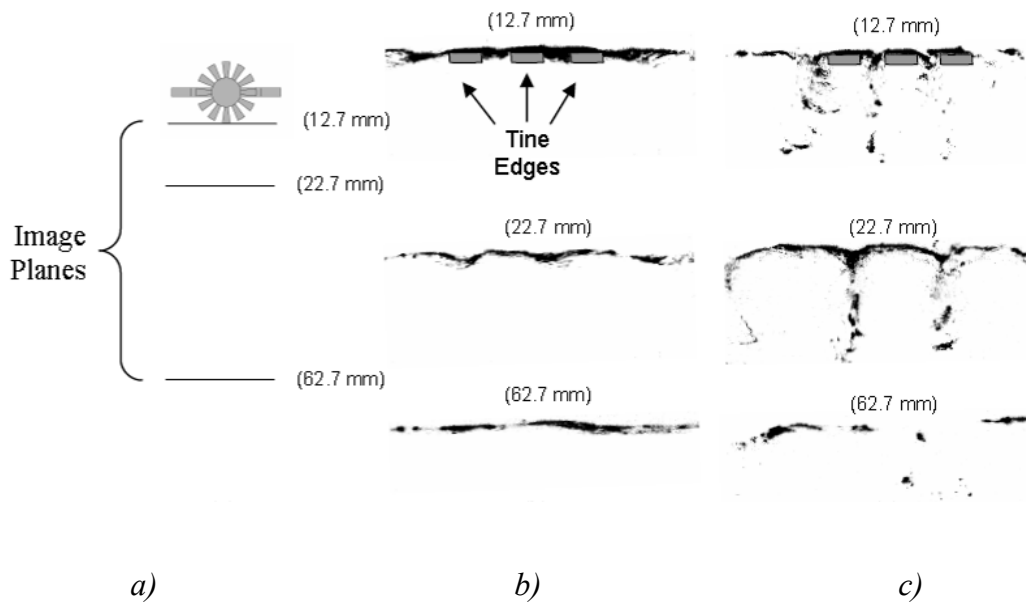


Figure 2-3: Inverted PLIF Images Depicting Flow through Sprinkler Spaces: (a) Top View of Measurement Locations, (b) Tined Nozzle, (c) Standard Nozzle [14]

Flow split measurements were conducted for the Standard Nozzles to provide the ratio between the flow deflected along the tines and through the spaces. This flow split can significantly affect the thickness of the streams and the associated break-up characteristics. The test setup, shown in Figure 2-4, consists of two separate plastic containers (40 L and 150 L) and a splitter plate, fabricated for an exact fit around each deflector and separating the small container from the large collection container. Simple measurement of the water volume collected in each container provides the flow split between the two streams.

Since these measurements are highly sensitive to the relative position of the splitting plate with respect to the spray, errors can be expected from splitting plate placement. Additionally, the pump fluctuation should also be taken into account as an error source. Finally, the volumes of water were measured by the graded tanks; thus, the accuracy of the measurements also relies on the precision of these volumetric scales. Nevertheless, these errors were minimized by averaging the results from three measurements, conducted at each pressure.

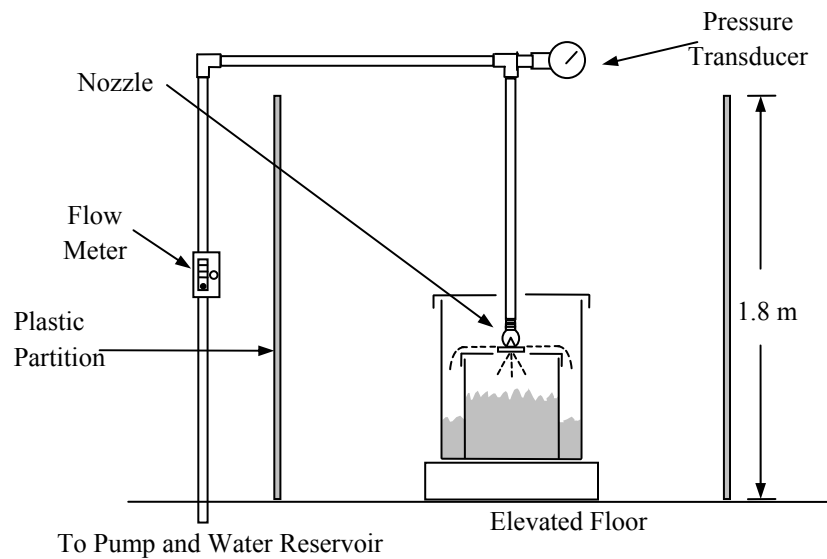


Figure 2-4: Flow Split Measurement Setup

The sheet break-up distance is one of the governing quantities that determine the characteristic drop size in the sprinkler atomization process. In this study, the sheet break-up distances over a range of operating pressures were experimentally measured

using short exposure time photographic and shadowgraphic techniques. Schematics of the experimental setup for these measurements are presented in Figures 2-5 and 2-6.

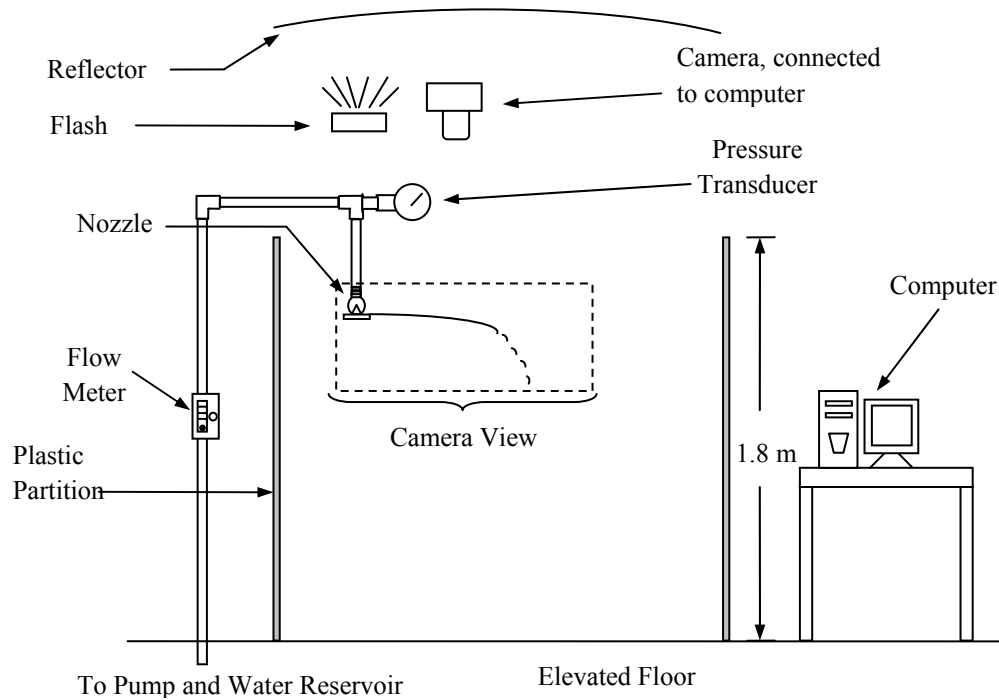


Figure 2-5: Horizontal Sheet Break-up Distance Measurements

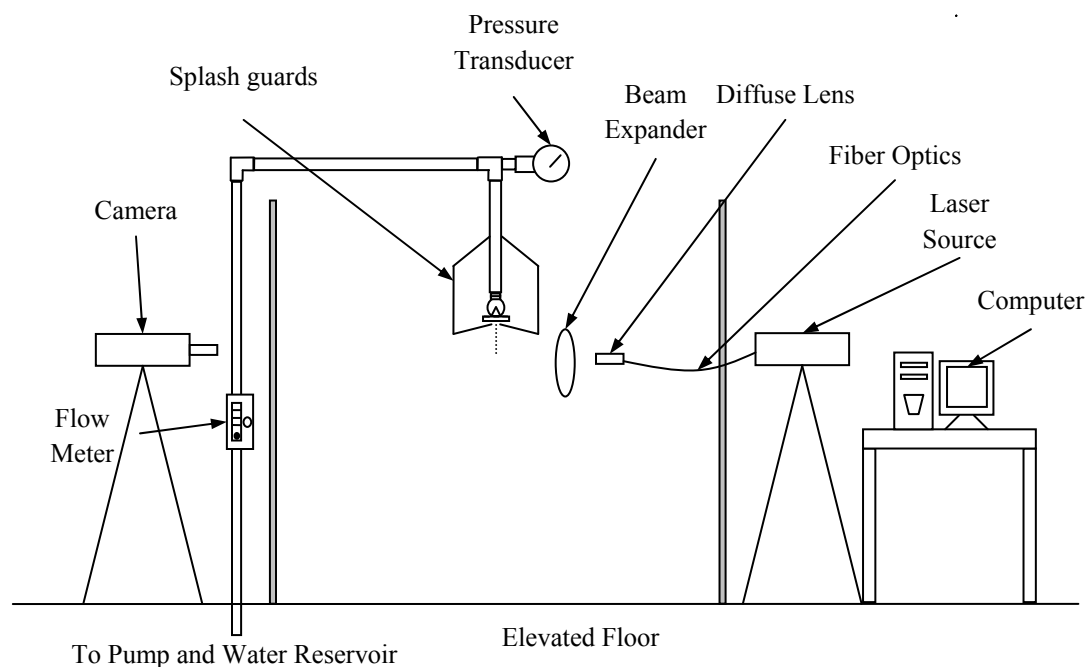
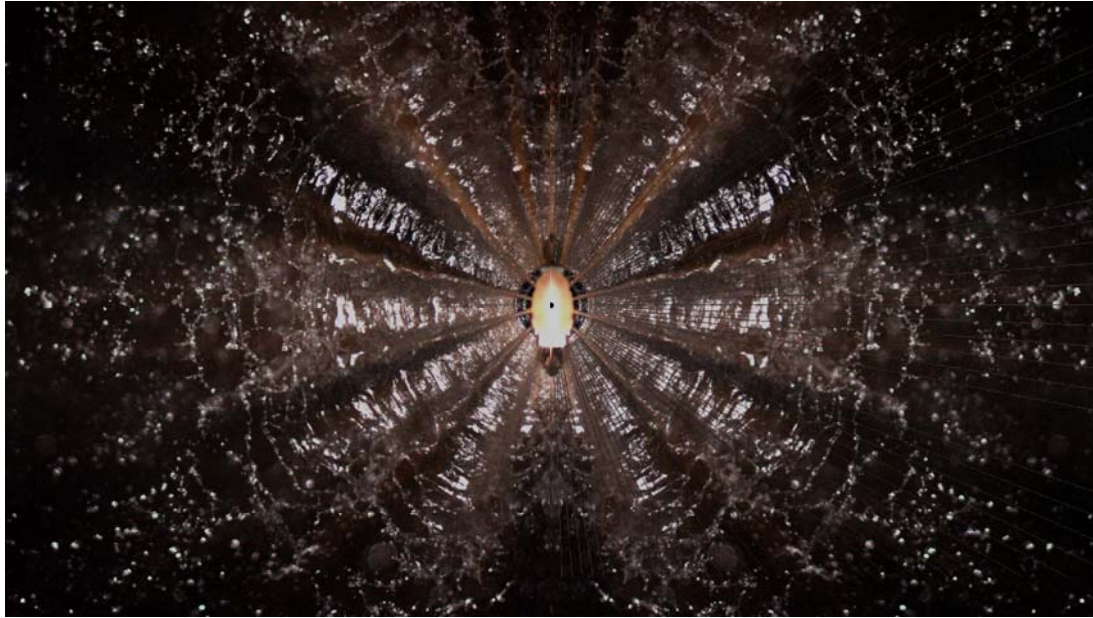


Figure 2-6: Vertical Sheet Break-up Distances Measurements and Flow Visualization Apparatus

For the short exposure time photographs, a Canon EOS 40D 10.1 Megapixels digital camera fitted with a 50 mm Canon f1.4 lens was mounted approximately 1 m above the nozzle and focused on the horizontal sheet formed parallel to the deflector. A Canon Speedlite 580EX II flash with discharge time of $7.8 \mu\text{s}$ was installed near the camera and bounced off a reflecting umbrella installed above the entire setup, to generate a diffuse light source for illuminating the liquid sheet. The image of the reflector on the sheet also helped to clearly distinguish the water streams from the black background below. Twenty images at each operating pressure were captured for all of the nozzles tested. In each image, break-up distances were determined at approximately 55 circumferential

stations, created by a set of rays that span from -90° to 90° with the increment of 2° . A sample of the images with and without the overlaid rays is shown in Figure 2-7. Additional images at different operating pressures can be found in Appendix B.



a)

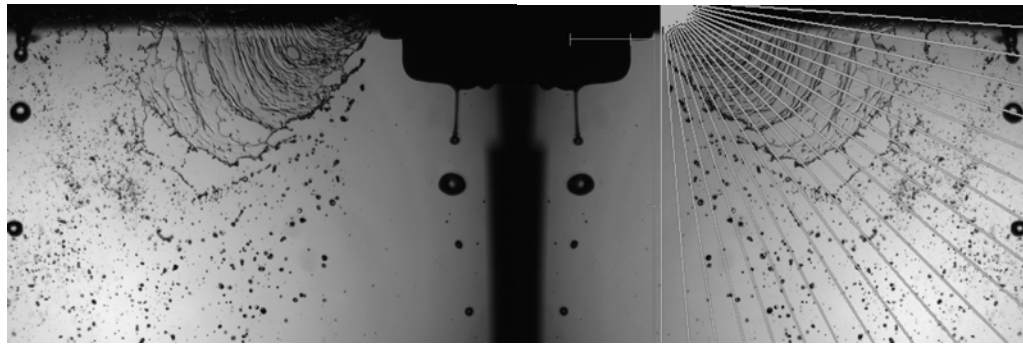
b)

Figure 2-7: Overhead Image for Break-up Distance Determination: a) Raw Image, b) Overlaid Image for Break-up Measurements

Using a LaVision Sizing Master shadowgraphy system described in Figure 2-6, the vertical sheets formed from the space streams were carefully studied. The shadowgraphy measurements provided a means to measure sheet structure and sheet break-up distance in the vertical orientation, which was not feasible with the direct imaging approach. A Double Pulsed Yttrium-Aluminum-Garnet (YAG) Laser was used to generate pairs of

532 nm laser pulses at the frequency of 3 Hz. The laser pulses were directed by a 1-meter fiber optic into a diffuser whose screen lit up with each pulse. This screen was then expanded by a Fresnel lens to approximately 200 mm. The images were captured utilizing a 4-Megapixel Image Pro X Charge Coupled Device (CCD) Camera, fitted with a 50 mm Canon f1.4 lens. The imaging region of the camera consisted of a field of view of approximately 150 mm square with a depth of field of about 28 mm. The discharge rates of the laser source and capture rate of the camera were synchronized by a computer to obtain double images of the spray (useful for velocity measurements), although only one of the images in the pair was used for break-up analysis.

A special set of splash guard partitions was fabricated for the sheet visualization and break-up distance measurements. These partitions allowed only one stream to enter the field of view of the shadowgraph camera. Twenty images were taken at each operating pressure for two Standard Nozzles having K-factors of 25.9 and 80.9 lpm/bar^{-1/2}. In each image, break-up distances were determined at 18 azimuthal stations sweeping a 90° angle with the origin located at the beginning of the space slot. A sample of these images is presented in Figure 2-8. Additional images taken at different operating pressure are presented in Appendix B.



a)

b)

Figure 2-8: Space Sheet Visualization: a) Raw Image Obtained with Shadowgraphy Technique, b) Overlaid Image for Break-up Measurements

The sheet break-up measurements rely on the orientation of the cameras, the accuracy of the calibration, and the human error during manually recording the break-up distances. Since the cameras were carefully installed, the error due to cameras orientation can be considered minimal. The calibration process also produces a negligible error because it was performed on known dimensions such as deflector diameter and nozzle frame, which are present in every frame. However, the human error during data recording can be significant, especially when the images become unclear at high pressure. Therefore, a large number of data points, taken in each frame, were used to calculate the average sheet break-up distances in order to minimize the effect of this error source.

Shadowgraphy technique was also utilized to provide detailed simultaneous measurements of drop size and velocity as depicted in Figure 2-9. After spatial

calibration of the field of view, drop sizes are easily determined using an edge detection algorithm provided with the LaVision Sizing Master software. A Particle Tracking Velocimetry (PTV) algorithm also included in the software uses the shadowgraph image pairs separated by a short time increment, approximately 100 ms for the measurements in this study, to track the displacement between adjacent similarly sized particles. The displacement determined from the calibrated images along with the separation time provides velocity information for every drop.

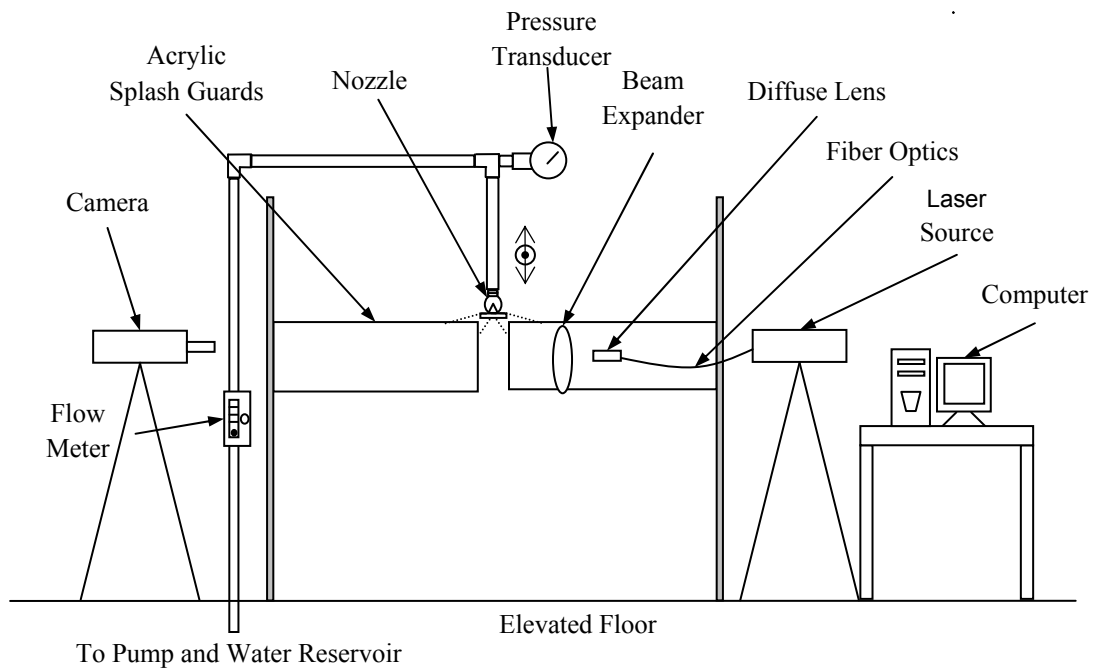


Figure 2-9: Drop Size and Velocity Measurement Apparatus

The acrylic splash guard partitions allowed only the desired portion (3 cm thick) of the spray to enter the focal plane of the camera where the shadows of the droplets on the

bright background were captured. For all nozzle configurations, drop size and drop velocity were measured simultaneously at several stations to cover the entire characteristic streams as shown in Figure 2-10. The locations in these measurements were obtained by traversing and rotating the nozzles with respect to the camera field of view. At each measurement location, 200 pairs of images were taken, providing size and velocity of approximately 20,000 – 100,000 drops after being post-processed. Subsequently, data after the break-up region (between 400 mm to 450 mm from the basis deflector edge and between 250 mm and 450 mm from the standard deflector edge) was used for analysis purposes.

Drop size and drop velocity data obtained by shadowgraphic technique is highly accurate. Nevertheless, its accuracy also depends on the images of the drops. When the density of the spray increases, the post process program is more likely to skip overlapping drops. On the other hand, if the spray is excessively blocked by the splash guards, reflected drops with altered velocities and diameters tend to enter the sample volume as well. Therefore, to mitigate this error, the splash guards were adjusted so that the thickness of the spray entering the camera field of view is roughly equal to the camera depth of view. This ensures the accuracy of the drop size and drop velocity once these quantities are recorded. Although unrecognized drops can still be observed in the post processed images, the large number of recognized drops is sufficient to represent the spray with little bias.

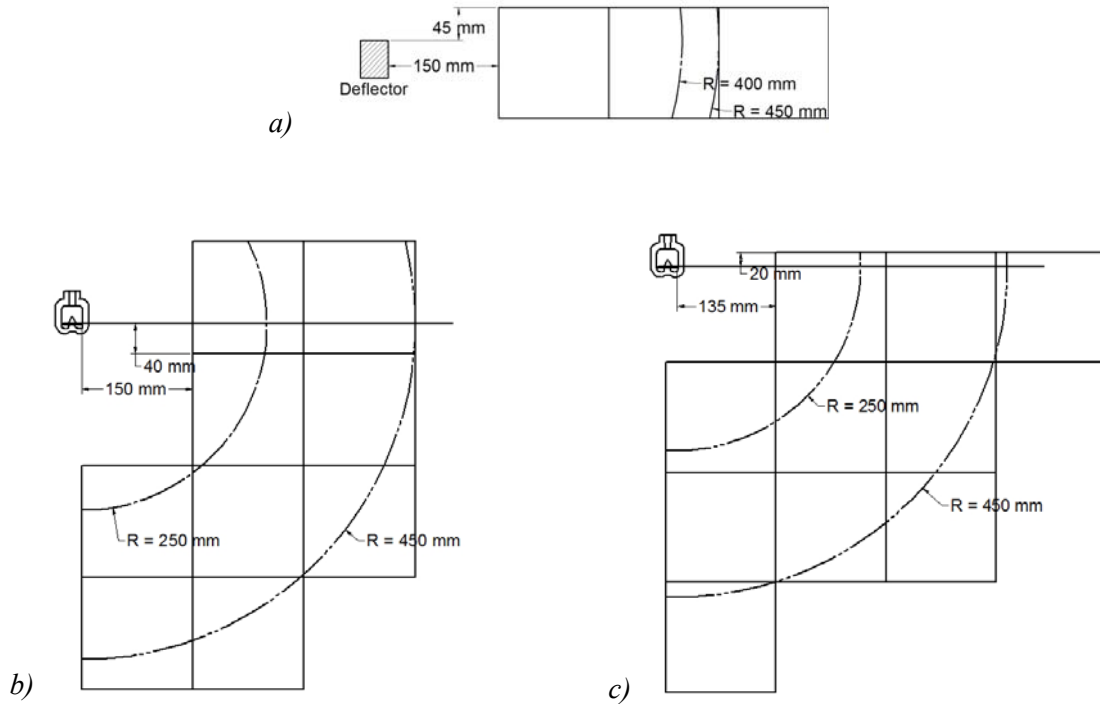


Figure 2-10: Measurement Locations: a) Basis Nozzle Measurements, b) Standard Nozzle Measurements – Tine Stream, c) Standard Nozzle Measurements – Space Stream

2.3. Scaling Laws

The atomization process for a liquid sheet formed on a flat horizontal surface can be described based on modeling ideas first proposed by Dombrowski and Hooper [2], Watson [20], and Ibrahim [24]. Their analyses have been adapted, integrated, and simplified by Ren to formulate scaling laws characterizing atomization in fire sprinklers [17]. In this study, these scaling laws were modified to include the sheet breakup and drop formation processes along the space and tine streams.

As the flow travels along the deflector, a boundary layer develops reducing the velocity of the developing film. Although the film thickness decreases as it travels radially outward along the deflector, the viscous interaction with the deflector decelerates the sheet resulting in a thicker sheet than that expected from inviscid flow. The sheet thickening factor at the edge of the deflector, $\beta = U_o / U_{sh}$, assumed to be the same for the horizontal and vertical sheets, can be expressed as

$$\beta = 1 + 0.0564 \frac{Re^{-1/5}}{\gamma} \left(\frac{D_d}{D_o} \right)^{9/5} \quad (2-1)$$

based on Watson's model [19] and Ren's analysis where Re is the jet Reynolds number of the jet, γ is the flow split factor, D_d is deflector diameter, and D_o is orifice diameter. The quantity γ describing the flow distribution between the tine and space streams deserves further discussion. This flow distribution quantity describes the ratio of the stream-wise flow split to the stream-wise geometric area split so that $\gamma_t = 1$ represents a deflector that geometrically balances the flow. When $\gamma_t < 1$, a greater proportion of flow is directed through the void spaces in the deflector resulting in a thinner tine stream. The tine flow split factor can be determined from

$$\gamma_t = \frac{Q_T / Q_{Total}}{n_t \theta_{tine} / 2\pi} \quad (2-2)$$

where the tine flow rate over the total flow rate is based on flow split measurements, n_t is the number of tines of the sprinkler, and θ_{tine} is the tine angle (22°). Similarly, the space flow split factor can be determined from

$$\gamma_s = \frac{Q_s / Q_{Total}}{n_s \alpha / 2\pi} \quad (2-3)$$

where n_s is the number of spaces of the sprinkler and α is the angle of the space sheet. This angle can be estimated using the boss angle of the sprinkler (56°). The sheet thickening and flow split factors, β and γ are critically important because they affect the sheet thickness and velocity which have leading order effects on the breakup process.

After leaving the deflector, the sheet thins as it moves radially outward. Figure 2-11 provides simplified descriptions of the sheets created by the tines and void spaces. Since the mass of the flow is conserved, the thickness of these sheets can be related to the radial location, sheet geometry, and the flow rate of the nozzle. The sheet thickness for the tine streams and space streams in terms of these quantities is given by $T_t = (\beta\gamma_t)(D_o^2 / 8r_d)/(r/r_d)$ and $T_s = (\beta\gamma_s)(D_o^2 / 8r_s)/(r/r_s)$, respectively.

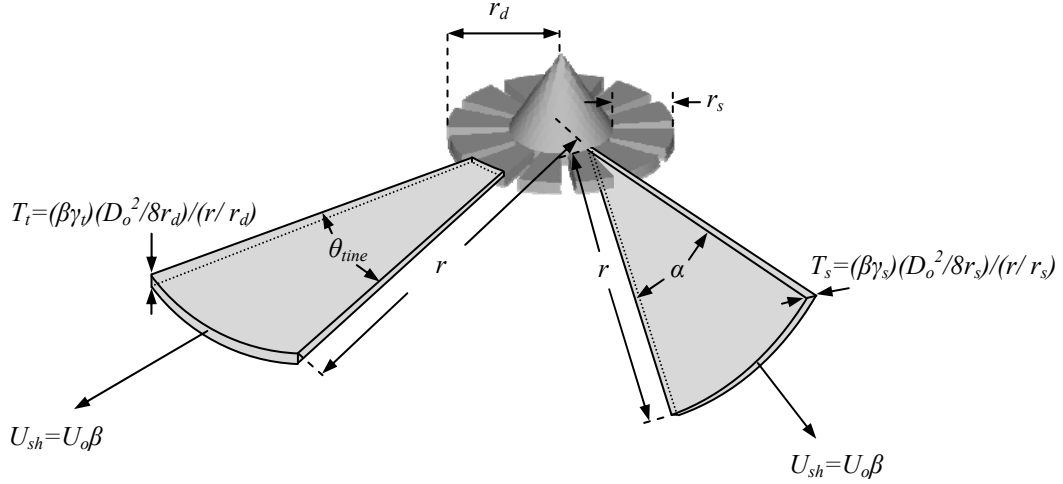


Figure 2-11: Sheets Geometry

In the scaling law developed by Ren, a sinuous wave dispersion equation was applied to the tine stream [17]. Shadowgraphy visualization of the space streams over a range of pressures from 0.69 to 2.76 bar confirms the presence of the sinuous wave pattern also on the space streams. As a result, sinuous wave dispersion equations were employed to describe sheet breakup from the space and tine streams. Since the break-up distances of these sheets can be computed in the same manner, in the following discussion, only the break-up distance of the horizontal sheet will be presented in details.

Based on wave dispersion theory, the growth of the sinuous wave on a thin inviscid sheet can be described by

$$\frac{\partial f}{\partial t} = \left(\frac{4r(\rho_a n U_{sh,tine}^2 - \sigma n^2)}{\rho_l D_d T_d} \right)^{\frac{1}{2}} \quad (2-4)$$

where T_d is the sheet thickness at the deflector edge. The critical wave number that leads to the break-up of the sheet can be found by maximizing the wave growth rate.

$$n_{crit,sh,tine} = \frac{\rho^* We}{2D_o \beta^2}. \quad (2-5)$$

Substituting Eq. 2-5 into Eq. 2-4 yields

$$\frac{\partial f}{\partial t} = \frac{\rho_a}{\rho_l} U_{sh,tine} \left(\frac{rWe}{2D_o r_d T_d \beta^2} \right)^{\frac{1}{2}}. \quad (2-6)$$

Recognizing that the radial location on the space sheet, r , can be expressed as $r = r_s + U_{sh}t$, and that $r_d T_d = (\gamma_t \beta / 8) D_o^2$, the wave growth rate equation can be written as

$$\frac{\partial f}{\partial r} = 2 \frac{\rho_a}{\rho_l} \left(\frac{rWe}{\gamma_t \beta^3 D_o^3} \right)^{\frac{1}{2}}. \quad (2-7)$$

Taking the integral of Eq. 2-7 where r varies from r_d to break-up distance, $r_{bu,tine}$ and f varies from zero to critical dimensionless sheet break-up wave amplitude $f_{o,t}$ yields an expression for the break-up location of the tine stream,

$$\frac{r_{bu,tine}}{r_d} = \left(1 + \frac{3}{4} \frac{f_{o,t}}{r_d^{3/2}} \left(\frac{\gamma_t \beta^3 D_o^3}{We} \right)^{\frac{1}{2}} \right)^{\frac{2}{3}}. \quad (2-8)$$

Further simplification assuming that the breakup distance is large with respect to the deflector diameter and normalizing by the orifice diameter results in

$$\frac{2r_{bu,tine}}{D_o} \sim X_{sheet,tine}^{-1/3} = \left[(\rho_a / \rho_l)^2 (f_{o,t})^{-2} (We / \beta^3 \gamma_t) \right]^{-1/3} \quad (2-9)$$

where $X_{sheet,tine}$ is the sheet break-up parameter for the tine stream which consists of a Weber number modified by nozzle factors affecting the viscous interaction with the deflector and the flow split ($We / \beta^3 \gamma_t$), and factors describing the density ratio and sheet stability, f_o . Similarly, the space stream breakup location can be expressed as

$$\frac{2r_{bu,space}}{D_o} \sim X_{sheet,space}^{-1/3} = \left[(\rho_a / \rho_l)^2 (f_{o,s})^{-2} (We / \beta^3 \gamma_s) \right]^{-1/3}. \quad (2-10)$$

The sheet break-up parameter, $X_{sheet,space}$, integrates nozzle geometry and injection conditions into a single scaling parameter based on wave dispersion theory for evaluation of sprinkler atomization measurements and models.

After the sheet breaks up, the water continues moving radially outwards in the form of ring-like ligaments. The mass of a ligament, right after disintegrating from the sheet, can be estimated based on mass conservation and dilatational wave break-up mechanism.

$$m_{lig} \approx 2\pi^2 \rho_l T_{bu,tine} \frac{r_{bu,sh,tine}}{n_{crit,sh,t}} \quad (2-11)$$

By assuming cylindrical shapes, the ligament diameter can be obtained after substituting the sheet thickness at the break-up location, $T_{bu,tine}$, and the critical wave number $n_{crit,sh,t}$.

$$d_{lig} = \left(\frac{\gamma_t \beta^3 D_o^3}{\rho^* r_{bu,tine} We} \right)^{\frac{1}{2}} \quad (2-12)$$

Since the ligament diameter and characteristic drop size are directly proportional, Eq. 2-9 can be substituted into Eq. 2-12 to formulate the drop size scaling law.

$$\frac{d_{v50,tine}}{D_o} \sim X_{drop,tine}^{-1/3} = \left[\left(\frac{\rho_a}{\rho_l} \right)^{1/2} f_{o,t} We / \beta^3 \gamma_t \right]^{-\frac{1}{3}} \quad (2-13)$$

where $X_{drop,tine}$ is the drop size scaling parameter for the tine stream which also consists of a Weber number modified by nozzle factors similar to the sheet scaling parameter $X_{sheet,tine}$. In the same manner, the characteristic drop size of the space stream can be formulated as

$$\frac{d_{v50,space}}{D_o} \sim X_{drop,space}^{-1/3} = \left[\left(\frac{\rho_a}{\rho_l} \right)^{1/2} f_{o,s} We / \beta^3 \gamma_s \right]^{-\frac{1}{3}} . \quad (2-14)$$

Chapter 3: Results and Discussions

The horizontal and vertical streams from pendant sprinkler configurations were carefully characterized in this project through a series of experiments, focused on the most essential stages of the atomization process. In this section, the experimental results will be presented and discussed in details. Additionally, they will be used to validate the modified scaling laws, presented in section 2.3.

3.1. Flow Splits

The flow rate along the tines and through the spaces of the sprinkler greatly influence the sheet thickness, sheet break-up distances, and characteristic drop sizes. The ratios between these two flows for Standard Nozzles were provided by a series of flow split measurements conducted in this study. The experimental results are presented in Table 3-1.

Table 3-1: Flow Split Measurements Results

D3 Nozzle (K-factor = 25.9 lpm/bar ^{-1/2})		
Pressure (bar)	Flow through Spaces (%)	Flow on Tines (%)
0.69	48.81	51.19
1.38	48.93	51.07
2.76	52.07	47.93

D3 Nozzle (K-factor = 80.7 lpm/bar ^{-1/2})		
Pressure (psi)	Flow through Spaces (%)	Flow on Tines (%)
0.69	43.40%	56.60%
1.38	46.00%	54.00%
2.76	44.95%	55.05%

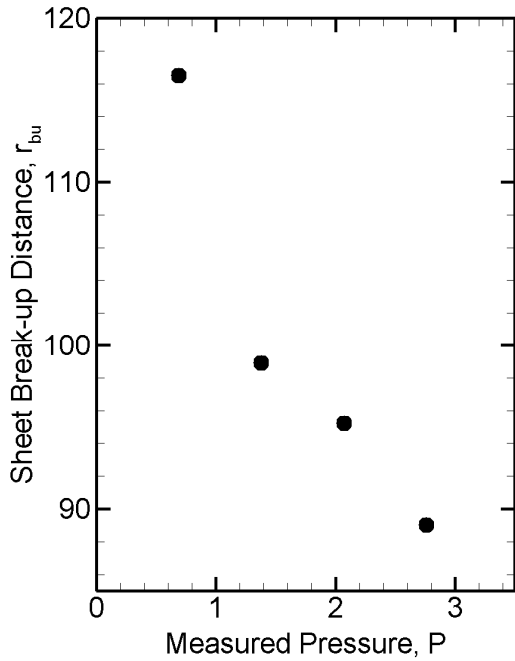
For each nozzle, the flow ratios remain relatively independent of the operating pressure. Small variations among pressures could also be the results of minor errors such as splitting plate position and pump fluctuation. The Standard Nozzle with K-factor of 25.9 lpm/bar^{-1/2} split the flow evenly between the tine and the space streams producing flow split factors, $\gamma_t = 0.68$ and $\gamma_s = 0.27$. Despite identical deflector geometry (i.e., identical tine and space surface area ratio), the Standard nozzle with K-factor of 80.7 lpm/bar^{-1/2} produces a flow bias toward the tine stream with $\gamma_t = 0.75$ and $\gamma_s = 0.24$. The only difference between the two nozzles, orifice diameters, suggests its role in altering the flow ratio. When the nozzle orifice size is increased, the additional flow meets increased resistance as it is forced through the void spaces, resulting in additional flow deflected along the tines.

3.2. Sheet Breakup Distances

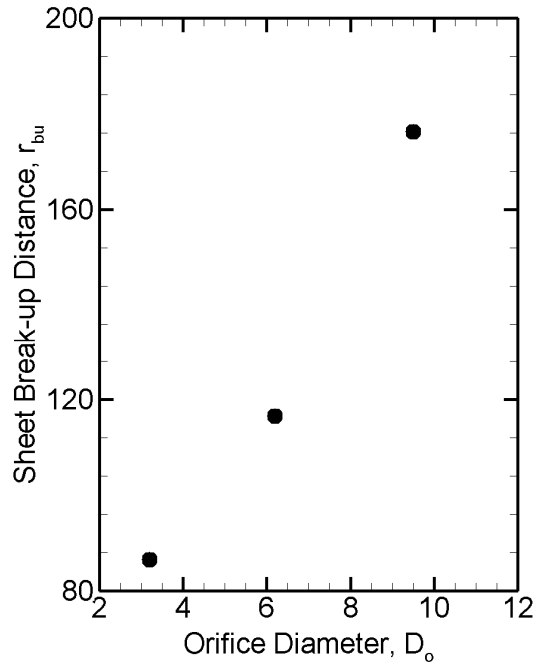
Employing short exposure time photography, the images of the horizontal sheets were obtained over a range of operating pressures. These digital images were analyzed after spatial calibration to determine the sheet break-up distances. The experimental results are presented in Table 3-2 along with the sheet break-up distances of the Basis Nozzles reported by Blum [14].

Table 3-2: Measured Horizontal Sheet Break-up Distances

	Measured Pressure (bar)	Basis Nozzle [14]			Standard Nozzle (Tine Stream)	
		D _o = 3.2	D _o = 6.2	D _o = 9.5	D _o = 6.2	D _o = 11.0
		r _d = 19	r _d = 19	r _d = 19	r _d = 12.7	r _d = 12.7
Sheet Breakup Distance, r_{bu} (mm)	0.69	86.50	116.50	176.27	65.40	86.60
	1.38	68.57	98.92	160.60	62.40	71.20
	2.07	65.43	95.23	N/A	57.40	N/A
	2.76	60.62	89.03	N/A	51.80	53.10



a)



b)

Figure 3-1: Observed Trends in Horizontal Sheet Break-up Distances: a) Sheet Break-up Distance vs. Pressure for Basis Nozzle with K-factor of $25.9 \text{ lpm/bar}^{-1/2}$, b) Sheet Break-up Distance vs. Orifice Diameter for Basis Nozzle at Similar Pressure (0.69 bar)

As the flow rate increases, the sheet thickness at a given location also increases. As a result, the sheet travels further before it becomes critically thin, delaying break-up. On the other hand, increasing operating pressure and associated initial flows accelerates the instability within the sheet, and therefore, enhances break-up. These two trends can be observed in Table 3-2 and Figure 3-1 where break-up distance was plotted against operating pressure and orifice diameter. It should be noted that the Standard Nozzle with K-factor of $25.9 \text{ lpm/bar}^{-1/2}$ shows a shorter sheet break-up distance compared to the Basis nozzle with a similar orifice diameter. This behavior suggests that sprinkler geometry such as the boss, spaces, and tines also play important roles in increasing sheet instability leading to earlier break-up.

Sheet break-up distances were normalized by the orifice diameter to account for the flow effect on sheet thickness and plotted against Weber number, which captures inertial effects as shown in Figure 3-2.

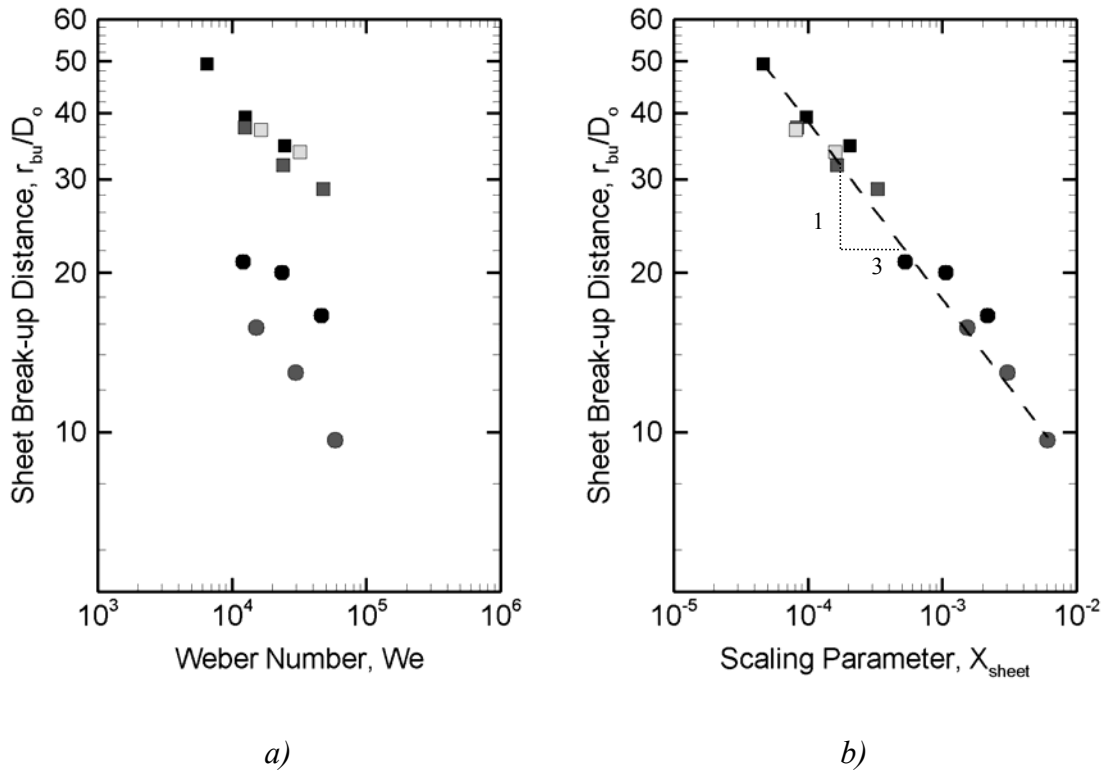


Figure 3-2: Horizontal Sheet Break-up Distances: a) Against Weber Number, b) Against Scaling Parameter. Standard Nozzles: ● $D_o = 6.2$ mm, ● $D_o = 11.0$ mm; Basis Nozzles: ■ $D_o = 3.2$ mm, ■ $D_o = 6.2$ mm, □ $D_o = 9.5$ mm

Although the sheet break-up distance follows a similar We trend, for a variety of nozzles, significant variation of the data is observed. This behavior suggests that despite its essential role, We does not govern the sheet break-up distances by itself. Due to its simplicity (i.e., absence of the boss, tines, and spaces), the Basis nozzles show a more consistent trend with respect to each other than the Standard nozzles. On the other hand, the two Standard Nozzles show a significant deviation from each other due to orifice diameter and the flow split factor differences.

The scaling parameter provides much better correlation with the dimensionless break-up distances for all nozzles. This parameter, $X_{sheet} = (\rho_a / \rho_l)^2 (f_o)^{-2} (We / \beta^3 \gamma)$, combines the effects of Weber number with others such as air liquid density ratio, flow split, thickening factor, and critical wave amplitude to successfully predict the sheet break-up distances. As a result, it is able to collapse the data from nozzles with different configurations. To compute X_{sheet} , the thickening factor was calculated, and the critical wave amplitude values were adjusted to best fit the scaling law for each nozzle. These values are presented in Table 3-3 and 3-4 below.

Table 3-3: Thickening Factor for Horizontal Sheet

	Measured Pressure (bar)	Basis Nozzle			Standard Nozzle (Tine Stream)	
		$D_o = 3.2$	$D_o = 6.2$	$D_o = 9.5$	$D_o = 6.2$	$D_o = 11.0$
		$r_d = 19$	$r_d = 19$	$r_d = 19$	$r_d = 12.7$	$r_d = 12.7$
Thickening Factor, β	0.69	1.57	1.14	1.07	1.23	1.07
	1.38	1.54	1.13	1.06	1.22	1.07
	2.76	1.50	1.13	N/A	1.20	1.06

Table 3-4: Critical Dimensionless Wave Amplitudes at Break-up for Various Nozzles

Nozzle		f_o
Basis Nozzles	$D_o = 3.2$ mm	7.1
	$D_o = 6.2$ mm	11.9
	$D_o = 9.5$ mm	15.4
Standard Nozzles, Horizontal Stream	$D_o = 6.2$ mm	5.0
	$D_o = 11.0$ mm	3.9
Standard Nozzles, Vertical Stream	$D_o = 6.2$ mm	4.4
	$D_o = 11.0$ mm	4.5

It is interesting to note that the critical dimensionless wave amplitude is directly proportional to the nozzle diameter for the Basis Nozzles, perhaps because the wave must grow larger and for a longer period of time to break the thicker sheet. On the other hand, the critical dimensionless wave amplitude did not change significantly for the Standard nozzles. This behavior suggests that the disturbances produced by the boss and spaces had a much greater effect on sheet break-up distances than that of the orifice diameter.

Employing shadowgraphy, the images of the vertical sheets from the two Standard Nozzles were attained. Similar to the horizontal sheets, these images were also manually analyzed to measure the sheet break-up distances. The break-up distances of the vertical sheets are shown in Table 3-5 along with those of the horizontal sheets.

Table 3-5: Measured Space Sheet Break-up Distances

	Measured Pressure (bar)	Standard Nozzle (Space Stream)		Standard Nozzle (Tine Stream)	
		$D_o = 6.2$	$D_o = 11.0$	$D_o = 6.2$	$D_o = 11.0$
		$r_s = 6.75$	$r_s = 6.75$	$r_d = 12.7$	$r_d = 12.7$
Sheet Breakup Distance, r_{bu} (mm)	0.69	41.73	57.24	65.40	86.60
	1.38	35.75	49.57	62.40	71.20
	2.76	33.25	43.73	51.80	53.10

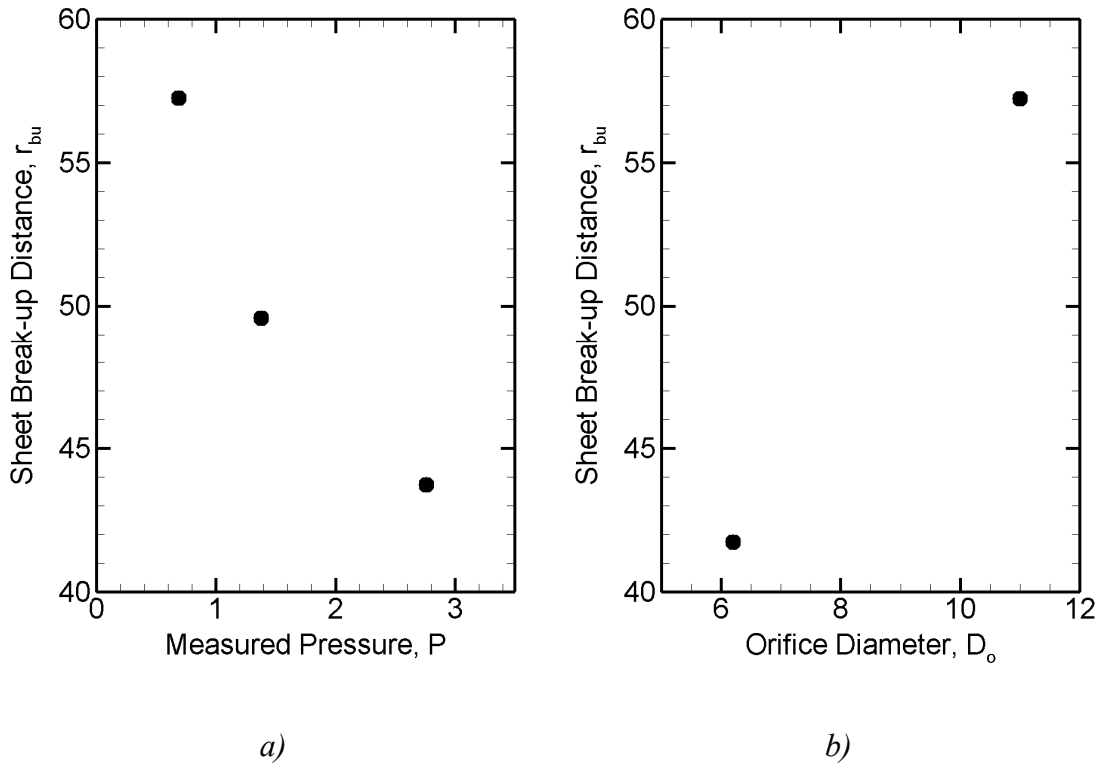


Figure 3-3: Observed Trends in Vertical Sheet Break-up Distances: a) Sheet Break-up Distance vs. Pressure for Basis Nozzle with K -factor of $80.7 \text{ lpm/bar}^{-1/2}$, b) Sheet Break-up Distance vs. Orifice Diameter for Standard Nozzles at Similar Pressure (0.69 bar)

The dimensionless break-up distances of the vertical sheets also follow the same trend observed with the horizontal sheets. The vertical sheet break-up distance is also directly proportional to orifice diameter and inversely proportional to injection pressure as shown in Figure 3-3.

The dimensionless sheet break-up distances were plotted against the Weber numbers and the scaling parameter X_{sheet} . These plots are presented in Figure 3-4 below.

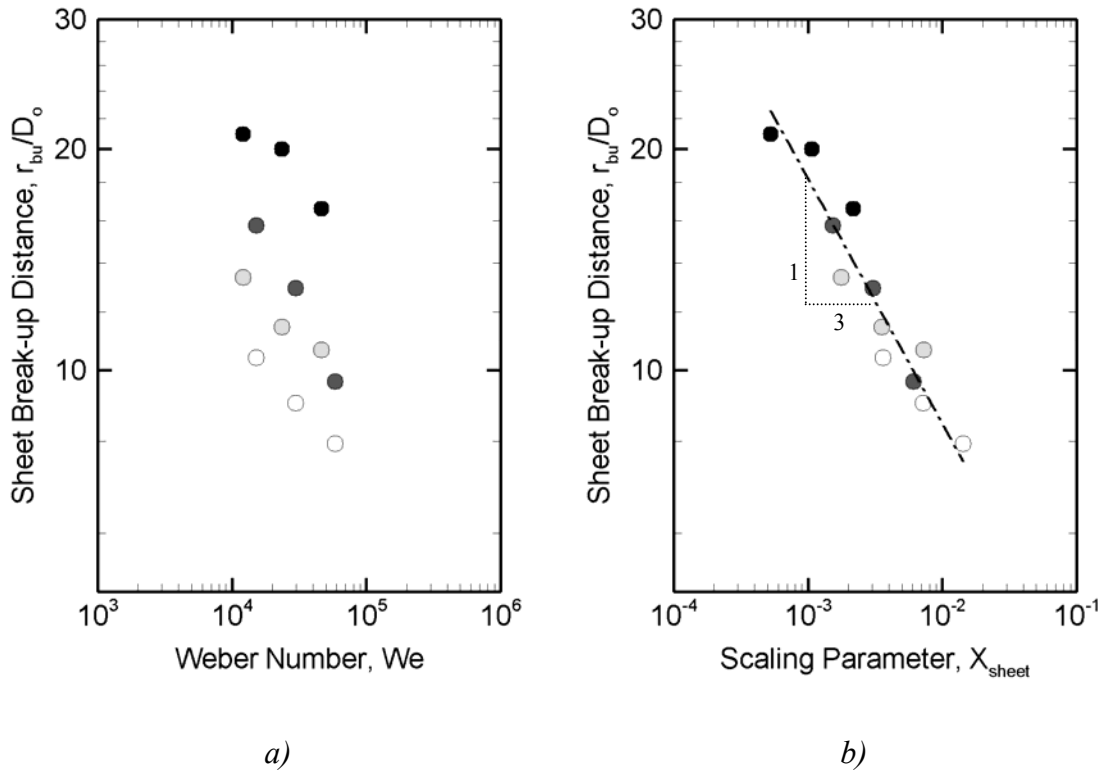


Figure 3-4: *Vertical Sheet Break-up Distances: a) Against Weber Number, b) Against Scaling Parameter. Standard Nozzles: \bullet $D_o = 6.2$ mm - Tine, \bullet $D_o = 11.0$ mm - Tine; \circ $D_o = 6.2$ mm - Space, \circ $D_o = 11.0$ mm - Space*

Similar to the horizontal stream, the Weber number cannot fully describe the sheet break-up distances of the vertical sheets. There is a large deviation between the break-up distances of the space sheet from the two Standard nozzles. However, by adding nozzle configuration factors to the Weber number, the scaling parameter can describe the experimental vertical sheet break-up distances with a single trend. For the similar reason, the scaling parameter also helped to collapse the data from two separate streams despite their configuration differences.

The critical wave amplitude values of the vertical sheets were also obtained to best fit the scaling law for each nozzle. These values have been presented in Table 3-4 above. The deviation between the two f_o values for the vertical sheets is even smaller than that of the horizontal sheet. Since the restriction of the space slot directs more flow horizontally outwards above the space slot, the vertical streams of the two nozzles remain fairly consistent while the added sprays between the tines create more disturbances to the horizontal sheets.

3.3. Characteristic Drop Size

3.3.1. Horizontal Stream Drop Size

Since sprays consist of a large collection of drop sizes, a characteristic drop size, based on an averaging scheme, is typically reported for spray studies. In this study, the overall flux-based volume median drop size d_{v50} was used to as the characteristic drop size of the spray. It is defined by indentifying the drop diameter where all smaller (or larger) drops contain 50% of the spray volume.

Drop size and velocity were measured simultaneously within the ranges of 250 mm to 450 mm from the deflector edge for the Standard Nozzles and 400 mm to 450 mm for the Basis Nozzles. Since these measurements covered the entire stream, the overall flux-based volume median drop sizes d_{v50} could be computed directly. These characteristic

drop sizes for the Basis Nozzles and the tine stream of the Standard Nozzles are presented in Table 3-6.

Table 3-6: Flux-based Characteristic Drop Sizes for Horizontal Streams

	Measured pressure (bar)	Basis Nozzle			Standard Nozzle (Tine stream)	
		D _o = 3.2	D _o = 6.2	D _o = 9.5	D _o = 6.2	D _o = 11.0
		r _d = 19	r _d = 19	r _d = 19	r _d = 12.7	r _d = 12.7
Characteristic drop size, d_{v50} (mm)	0.69	0.68	0.86	1.15	0.97	1.29
	1.38	0.54	0.85	1.05	0.76	1.17
	2.76	0.57	0.72	1	0.56	0.84

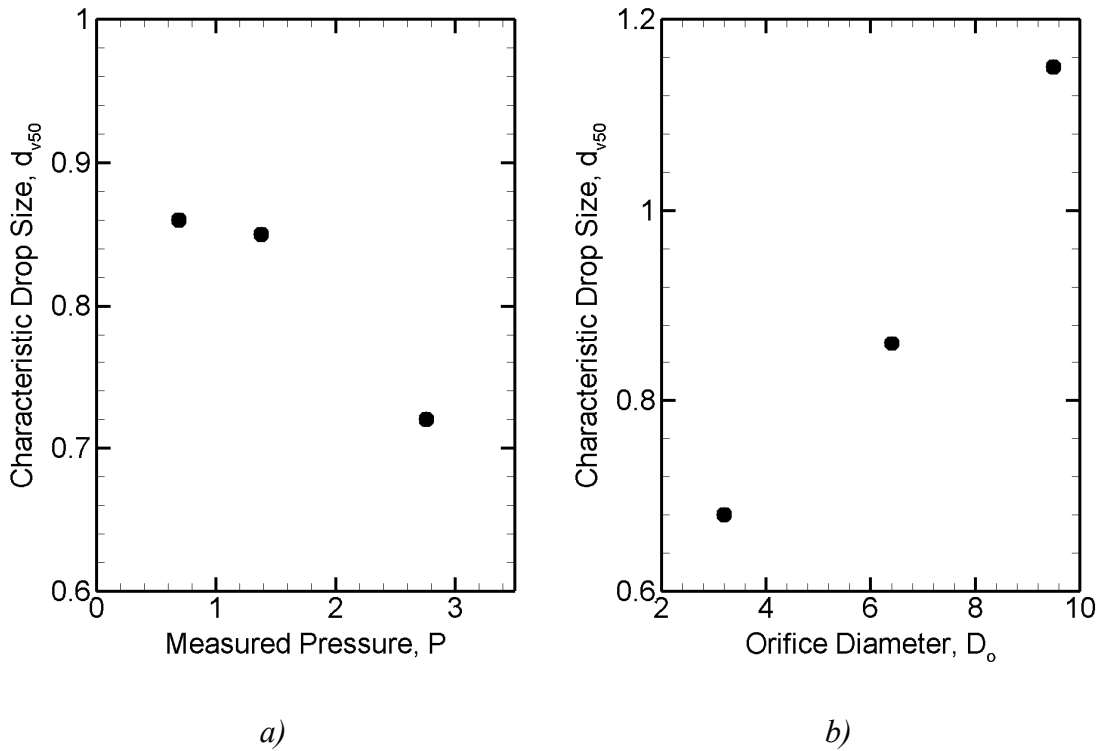


Figure 3-5: Observed Trends in Horizontal Stream Characteristic Drop Size: a) Drop Size vs. Pressure for Basis Nozzle with K-factor of $25.9 \text{ lpm}/\text{bar}^{-1/2}$, b) Drop Size vs. Orifice Diameter for Basis Nozzle at Similar Pressure (0.69 bar)

Similar to break-up distances, the characteristic drop diameter is also inversely proportional to the injection pressure and directly proportional to orifice diameter. This trend can be observed in Table 3-6 and Figure 3-5 for both Basis and Standard Nozzles. For a similar orifice diameter, the Standard Nozzle shows a slightly smaller volume median drop size compared to that of the Basis Nozzle because of the flow split effect that produces a thinner sheet.

The characteristic drop sizes were plotted against Weber number and scaling parameter X_{drop} . They are presented in Figure 3-6 below.

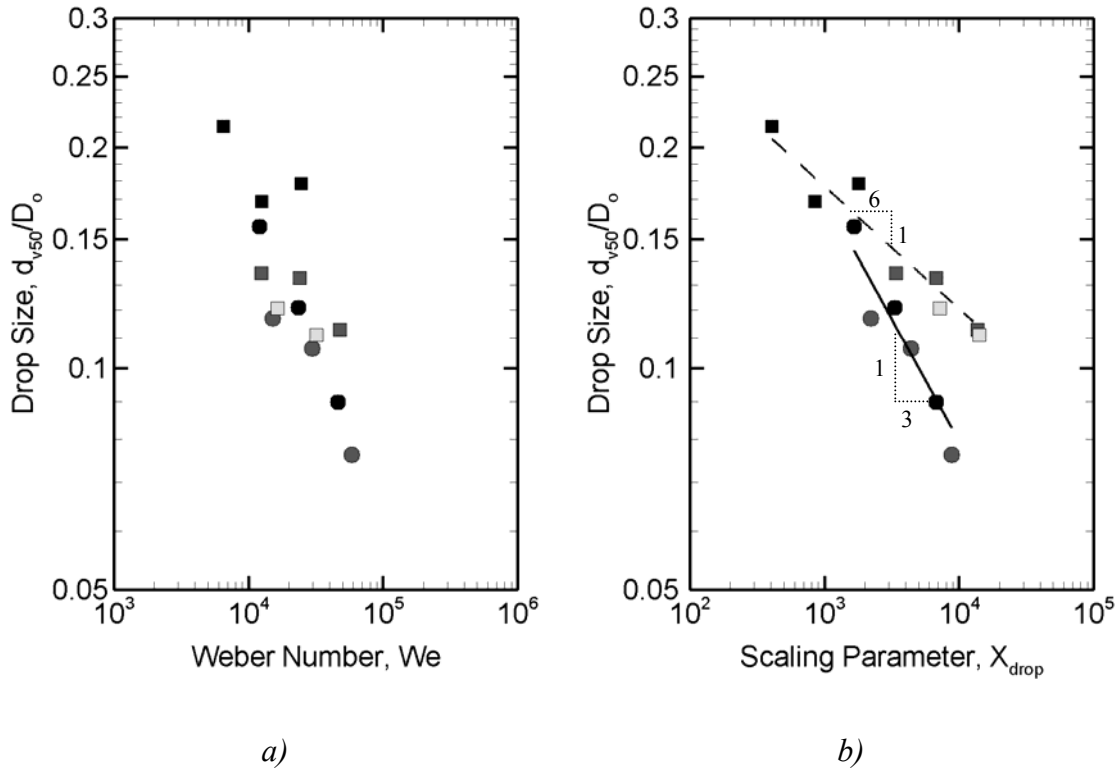


Figure 3-6: Horizontal Stream Characteristic Drop Sizes: a) Against Weber Number, b) Against Scaling Parameter. Standard Nozzles: ● $D_o = 6.2$ mm, ● $D_o = 11.0$ mm; Basis Nozzles: ■ $D_o = 3.2$ mm, ■ $D_o = 6.2$ mm, □ $D_o = 9.5$ mm

The characteristic drop sizes of the Basis Nozzles and the time stream of the Standard nozzles show significant scatter when they are plotted against the Weber Number. Although a common trend can be observed for the two Standard nozzles, the Basis Nozzles characteristic drop sizes appear that they follow three separate trends. On the other hand, the scaling parameter helps to collapse the Basis and Standard Nozzles data along two trends as demonstrated in Figure 3-6b. The dimensionless characteristic drop sizes from the time of the Standard nozzles show a good agreement with the expected $We^{-1/3}$ scaling law. However, a $We^{-1/6}$ scaling law can be observed for the Basis Nozzles data instead. Since the sinuous wave growth was visually observed on all the sheets, this deviation from the $We^{-1/3}$ scaling law must have come from the prediction of drop formation process. In other words, it suggests that ligament break-up did not occur for these Basis nozzles. As a result, the scaling law overestimates the influence of Weber number on the characteristic drop size formed by rim break-up mode in these nozzles. Similar observation was also reported in Blum's [14] and Ren's studies [17]. More analysis is needed to address the atomization process of these nozzles.

3.3.2. Vertical Stream Drop Size and Velocity

Similar to the horizontal stream, the overall flux-based volume median drop sizes of the vertical stream were obtained from drop size and drop velocity measurements. These characteristic drop sizes are presented in Table 3-7 along with its horizontal counterparts for comparison purposes.

Table 3-7: Flux-based Characteristic Drop Sizes for Vertical Streams

	Measured Pressure (bar)	Standard Nozzle (Space stream)		Standard Nozzle (Tine stream)	
		D _o = 6.2	D _o = 11.0	D _o = 6.2	D _o = 11.0
		r _d = 12.7	r _d = 12.7	r _d = 12.7	r _d = 12.7
Characteristic drop size, d_{v50} (mm)	0.69	0.91	1	0.97	1.29
	1.38	0.63	0.83	0.76	1.17
	2.76	0.43	0.75	0.56	0.84

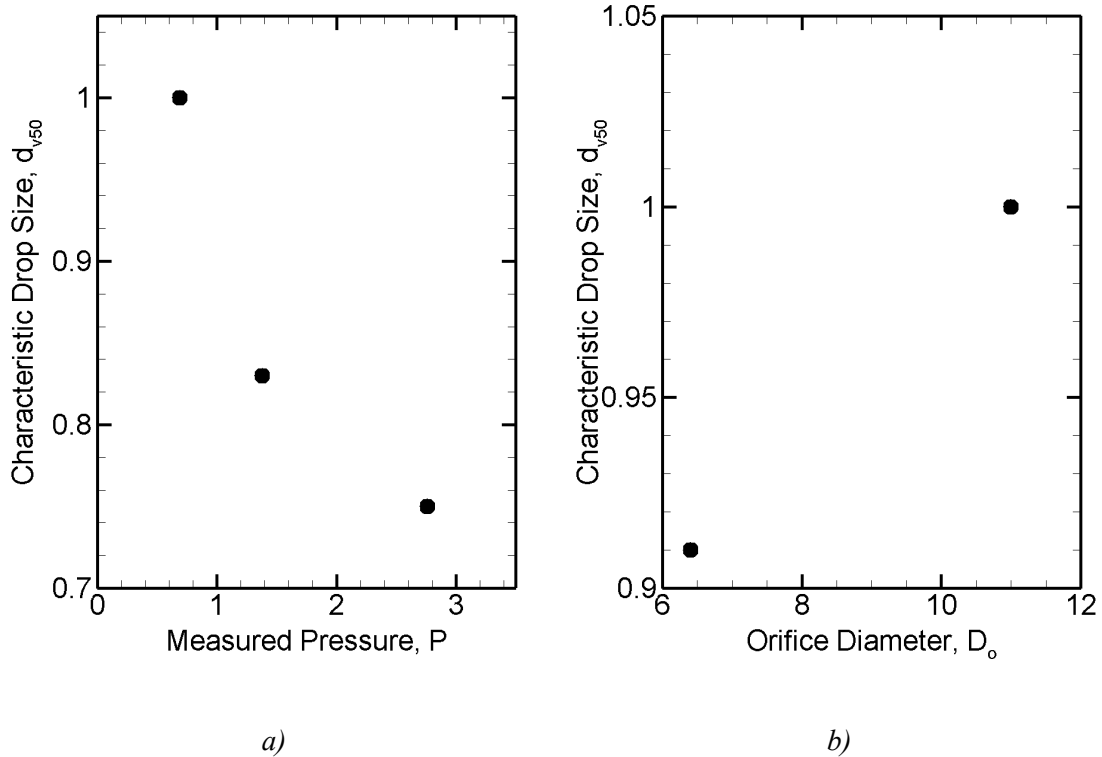


Figure 3-7: Observed Trends in Vertical Stream Characteristic Drop Size: a)

Drop Size vs. Pressure for Basis Nozzle with K-factor of 80.7 lpm/bar^{-1/2}, b) Drop Size vs.

Orifice Diameter for Basis Nozzle at Similar Pressure (0.69 bar)

The effects of operating pressure and orifice size on the characteristic drop size of the vertical stream are comparable to the horizontal stream. Drop size increases with increasing orifice and decreasing operating pressures as shown in Figure 3-7. Additionally, for the same nozzle, the characteristic drop sizes of the vertical stream appear smaller than that of the horizontal stream at any given pressure, especially for the Standard nozzle with K-factor of $80.7 \text{ lpm/bar}^{-1/2}$. The smaller amount of flow going through the spaces compared to the tines of the larger nozzle results in a thinner sheet, and therefore, smaller characteristic drop size.

The characteristic drop sizes of the two streams were also plotted against Weber number and the drop scaling parameter X_{drop} . The plots are presented in Figure 3-8 below.

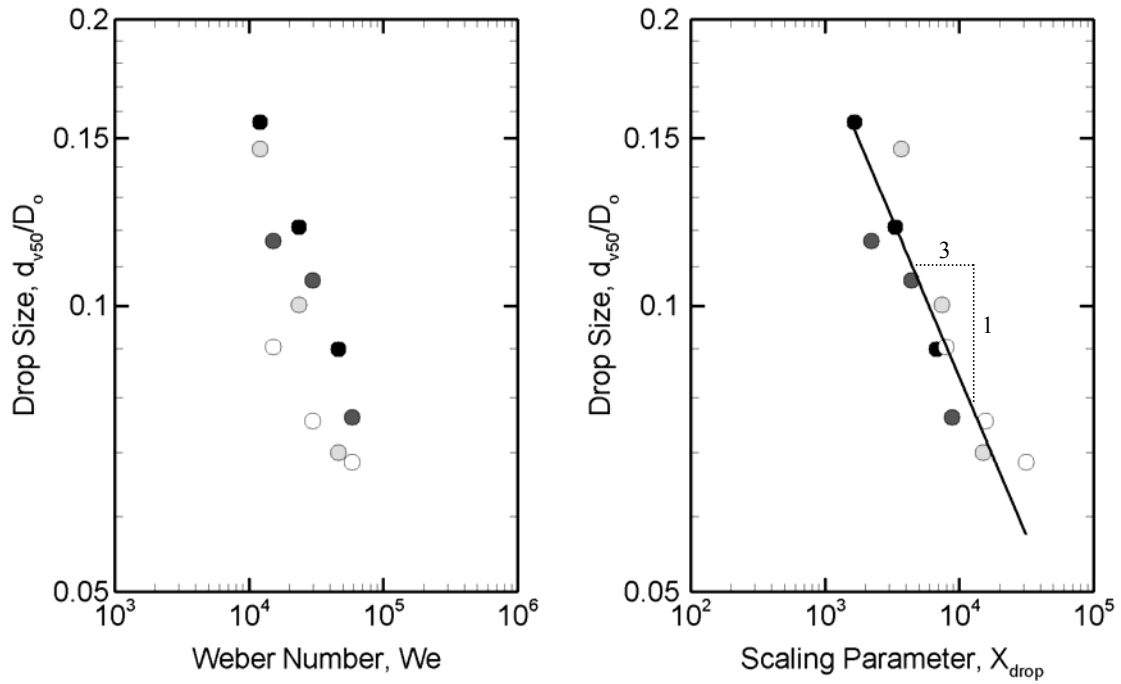


Figure 3-8: Vertical Stream Characteristic Drop Sizes: a) Against Weber Number, b) Against Scaling Parameter. Standard Nozzles: ● $D_o = 6.2$ mm - Tine, ● $D_o = 11.0$ mm - Tine; ● $D_o = 6.2$ mm - Space, ○ $D_o = 11.0$ mm - Space

The advantage of combining nozzle configuration factors that influence the atomization process into the Weber number is demonstrated again in Figure 15. The scaling parameter better predict the characteristic drop sizes from both horizontal and vertical streams since the configuration differences were already taken into account.

Chapter 4: Conclusions

A series of experiments were conducted to study the stream-wise discharge characteristics of fire suppression nozzles having geometry similar to pendant sprinklers. The measured spray characteristics were compared to that of a simplified reference nozzle consisting of a jet impinging on a solid circular deflector (i.e. without tines or void spaces). The flow split, sheet break-up, drop size, and velocity were quantified in a comprehensive set of detailed atomization measurements. Stream-wise analysis of the measured atomization behavior was performed using scaling laws to evaluate the effects of sprinkler geometry and injection conditions.

The flow split measurements demonstrated the effect of sprinkler geometry on the relative proportions of stream-wise flow and the associated sheet thickness. For similar deflector geometries, flow restrictions in the void spaces will direct more flow outward along the tines in larger higher flowing nozzles. For example, the larger Standard Nozzle directed more flow along the tines (55% compared to the 50% of the smaller nozzle).

Short exposure time photography and shadowgraphy were performed to visualize and quantify the topology of the horizontal tine stream and vertical space stream, respectively. Similar growing sinuous wave patterns leading to sheet break-up were observed on both horizontal and vertical sheets. Generally, the sheet break-up distances follow the $We^{-1/3}$ scaling law, yet the Weber number alone is unable to completely describe the various trends observed between different nozzles. To better describe the sheet break-up process, a modified Weber number for the sheet break-up distances was developed by integrating nozzle configuration and environmental effects into the

traditional Weber number describing injection conditions. This modified Weber number completely describes the sheet break-up distances for the Basis and Standard Nozzles (tine and space streams) in terms of a single trend line.

Drop sizes and drop velocities were obtained using a quantitative shadowgraphy technique. Stream-wise characteristic drop sizes showed a strong dependence on Weber number; however, a wide significant data scatter was still observed among streams and nozzles. Consequently, similar to the sheet break-up process, a modified Weber number was developed by including additional factors influencing drop formation. The results showed that the characteristic drop sizes from both the Standard Nozzle tine and space streams are well predicted by this modified Weber number following the expected $We^{-1/3}$ scaling law. Interestingly, the Basis Nozzle characteristic drop sizes over a range of sizes and injection conditions follow a single trend with respect to the modified Weber number, but possess a distinctly different scaling ($\sim We^{-1/6}$) than the standard nozzle. Similar observations were noted in Blum's [13] and Ren's [16] studies. The weaker Weber number scaling suggests that the Basis Nozzle atomization process is somehow fundamentally different than that of the Standard Nozzle [16]. More studies are needed develop physical models capable of describing the unique atomization mechanisms producing the different scaling laws observed for the Basis and Standard Nozzles.

Appendices

Appendix A: Inlet Section Characterization

The diagram of the inlet section is shown in Figure A1. Its geometries are presented in Table A1 as well.

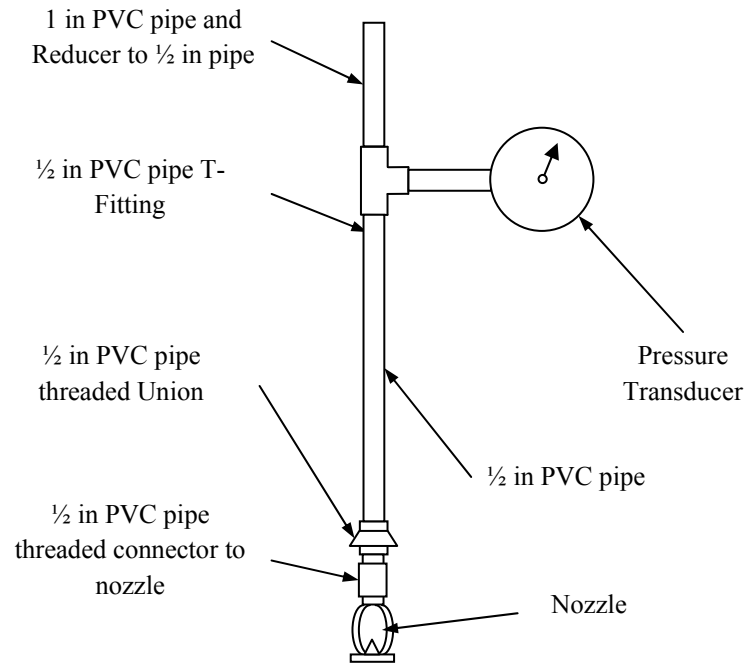


Figure A1: Inlet Diagram

Table A1: Inlet Components Geometries

Pipe	
Pipe Length (m)	0.4
Pipe Diameter (m)	0.015
Fittings	
Type	1 T connector; 3 Threaded unions
Total Fittings Length (m)	0.07

Flow tests were conducted for two nozzles with known K-factors. The average flow rates were obtained from three measurements, taken at each measured pressure. The results are presented in Table A2 below.

Table A2: Flow Tests Results

Measured Pressure (bar)	Nozzle with K = 80.7 lpm·bar ^{-1/2}	Nozzle with K = 43.2 lpm·bar ^{-1/2}
	Flow Rate (m ³ /s)	
0.69	9.19E-04	5.41E-04
1.38	1.31E-03	7.80E-04
2.76	1.87E-03	1.11E-03

From these flow rates and the nozzles K-factors, injection pressures were computed as

$$P_{injection} = \left(\frac{Q}{K} \right)^2 \quad (A-1)$$

These pressures were compared to the measured values, obtained from the pressure transducer, to determine the total pressure loss in the inlet section. This pressure loss consists of two main portions, the frictional loss in the pipe and the losses at the fittings.

Pressure losses due to friction in pipe were directly calculated based on the flow measured.

$$\Delta P_{friction} = f \frac{l_{pipe}}{D_{pipe}} \frac{\rho_l U_{pipe}^2}{2} \quad (A-2)$$

In equation A-2, f is the friction factor in the pipe obtained for each flow condition by solving the following equation

$$\frac{1}{\sqrt{f}} + 2.0 \log \left(\frac{\varepsilon / D_{pipe}}{3.7} + \frac{2.51}{\text{Re}_{pipe} \cdot \sqrt{f}} \right) = 0 \quad (\text{A-3})$$

where ε is the factor, accounting for pipe roughness. For PVC pipe, this factor is approximately zero. Thus, equation A-3 was simplified as

$$\frac{1}{\sqrt{f}} + 2.0 \log \left(\frac{2.51}{\text{Re}_{pipe} \cdot \sqrt{f}} \right) = 0 \quad (\text{A-4})$$

The pressure losses at the fittings were then computed by the following equation.

$$\begin{aligned} \Delta P_{fittings} &= P_{measured} + \Delta P_{elevation} - P_{injection} - \Delta P_{friction} \\ \Rightarrow \Delta P_{fittings} &= P_{measured} + \rho g (l_{pipe} + l_{fittings}) - P_{injection} - \Delta P_{friction} \end{aligned} \quad (\text{A-5})$$

These pressure losses were plotted against $0.5 \rho_l U_{pipe}^2$ to determine the coefficient of pressure losses in the fittings. The results are presented in Figure A2 below. The slope of the straight line going through the scattered data points is the coefficient.

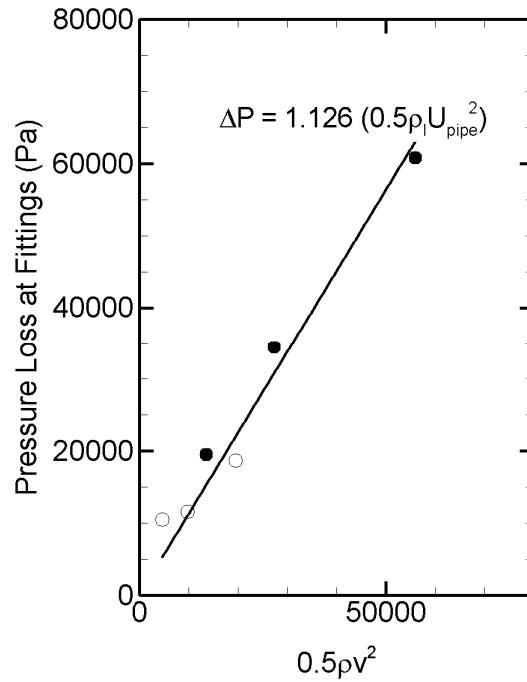


Figure A2: Pressure Loss Coefficient at Fittings

This pressure loss coefficient was then used to recalculate the K-factor of the nozzle and check against the known K-factor. The errors were found in the order of 2.6% to 4.8%. These negligible errors show confidence in the calculation of pressure loss coefficient.

By using this pressure loss coefficient, the injection pressure at any given measured pressure and nozzle K-factor could be calculated. These injection pressures are presented in Table A3.

Table A3: Calculated Injection Pressures

Injection Pressure Table (bar)						
Nozzle K-Factor, lpm/bar ^{1/2}	Measured Pressure (bar)					
	0.69	1.38	2.07	2.76	3.45	4.14
7.2	0.73	1.42	2.11	2.79	3.48	4.17
25.9	0.70	1.35	2.01	2.67	3.33	3.98
43.2	0.64	1.25	1.86	2.47	3.08	3.69
49.0	0.62	1.21	1.80	2.39	2.98	3.57
80.7	0.50	0.97	1.45	1.92	2.40	2.88

The pressure losses were also compared to the measured pressures. These comparisons are shown in Table A4.

Table A4: Pressure Losses Percentage at Given Measured Pressure

Nozzle K-Factor, lpm/bar ^(0.5)	Measured Pressure (bar)					
	0.69	1.38	2.07	2.76	3.45	4.14
7.2	-6.2%	-2.9%	-1.8%	-1.2%	-0.9%	-0.7%
25.9	-1.3%	1.8%	2.8%	3.2%	3.5%	3.7%
43.2	6.7%	9.3%	10.1%	10.5%	10.7%	10.9%
49.0	9.8%	12.3%	13.0%	13.4%	13.6%	13.7%
80.7	27.9%	29.6%	30.1%	30.3%	30.4%	30.4%

* Positive values indicate pressure loss and negative values indicate pressure gain

Appendix B: Spray Images

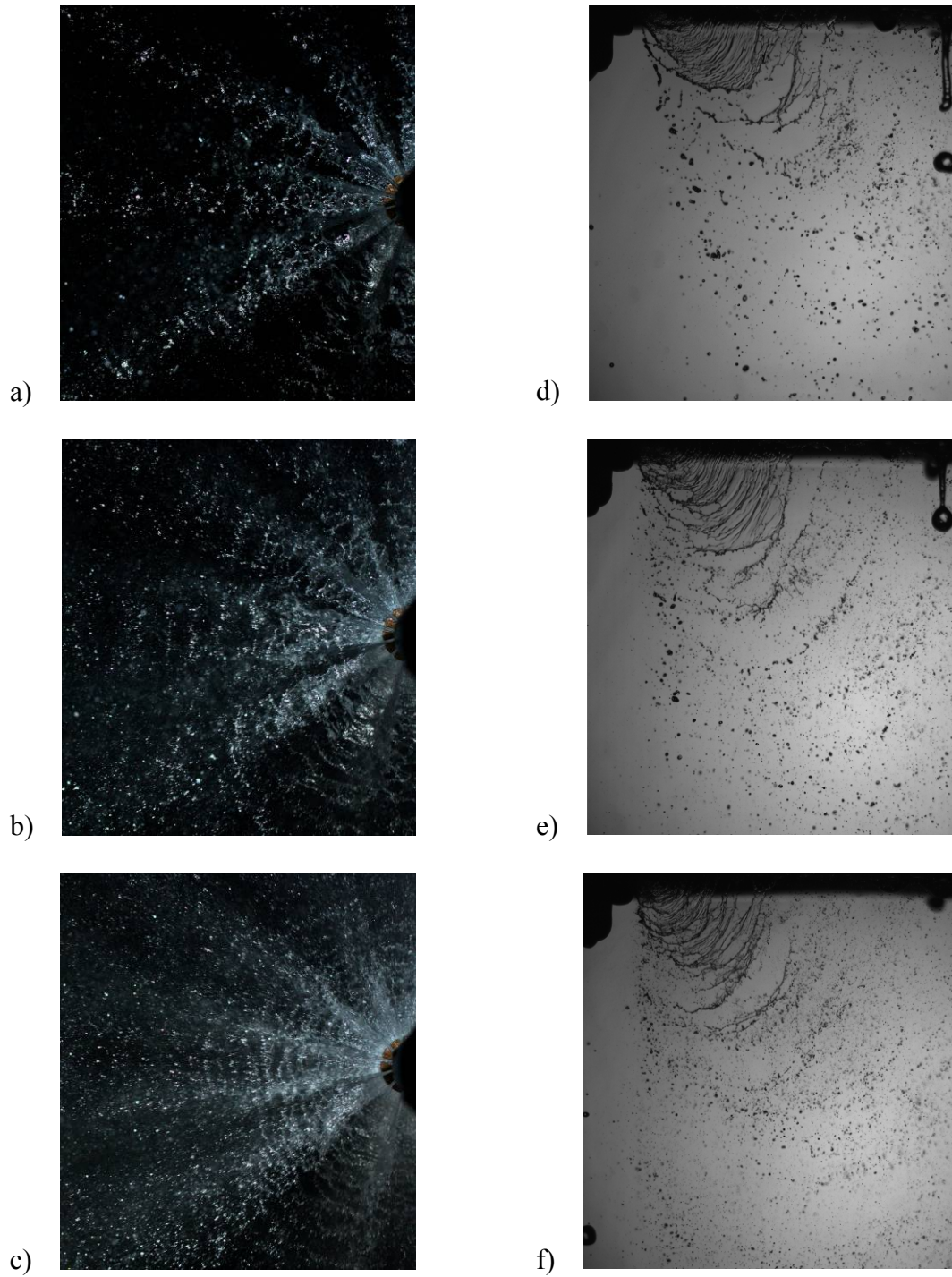


Figure B1: Sheet Break-up Measurements

Bibliography

- [1] Grant, G., Brenton, J., and Drysdale, D., "Fire Suppression by Water Sprays," *Progress in Energy and Combustion Science*, Vol. 26, pp. 79-130, 2000.
- [2] Dombrowski, N., Hooper, P. C., "The Effect of Ambient Density on Drop Formation in Sprays", *Chemical Engineering Science*, Vol. 17, pp. 291-305, 1962.
- [3] Huang, J. C. P., "The Break-up of Axisymmetric Liquid Sheets", *Journal of Fluid Mechanics*, Vol. 43, pp. 305-319, 1970.
- [4] Prahl, J. M., Wendt, B., "Discharge Distribution Performance for an Axisymmetric Model of a Fire Sprinkler Head", *Fire Safety Journal*, Vol. 14, pp. 101-111, 1988.
- [5] Clanet, C., Villermaux, E., "Life of a Smooth Liquid Sheet", *Journal of Fluid Mechanics*, Vol. 462, pp. 307-340, 2002.
- [6] Villermaux, E., Clanet, C., "Life of a Flapping Liquid Sheet", *Journal of Fluid Mechanics*, Vol. 462, pp. 341-363, 2002.
- [7] Dundas, P. H., "Technical Report Optimization of Sprinkler Fire Protection the Scaling of Sprinkler Discharge: Prediction of Drop Size", *Factory Mutual Research Corporation*, Norwood, MA, June 1974.
- [8] Yu, H.Z., "Investigation of Spray Patterns of Selected Sprinklers with the FMRC Drop Size Measuring System", *First International Symposium on Fire Safety Science*, New York, pp. 1165-1176, 1986.
- [9] Widmann, J. F., Sheppard, D. T., and Lueptow, R. M., "Non-Intrusive Measurements in Fire Sprinkler Sprays", *Fire Technology*, Vol. 37, pp. 297-315, 2001.
- [10] Widmann, J. F., "Phase Doppler Interferometry Measurements in Water Spray Produced by Residential Fire Sprinklers", *Fire Safety Journal*, Vol. 36, pp. 545-567, 2001.
- [11] Sheppard, D. T., Gandhi, P.D., "Understanding Sprinkler Sprays: Trajectory Analysis" NISTIR 6561, *National Institute of Standards and Technology*, Gaithersburg, MD, 2000.
- [12] Sheppard, D. T., "Spray Characteristic of Fire Sprinkler", NIST GCR 02-838, *National Institute of Standards and Technology*, Gaithersburg, MD, 2002.
- [13] Putorti A.D., "Simultaneous Measurements of Drop Size and Velocity in Large-Scale Sprinkler Flow Using Particle Tracking and Laser-Induced Fluorescence", NIST GCR-861, *National Institute of Standards and Technology*, Gaithersburg, MD, 2004.
- [14] Blum, A., Marshall, A. W., "Discharge Characteristics of Canonical Sprinkler Sprays", M.S. Thesis, *University of Maryland-College Park*, 2006.

- [15] Wu, D., “Atomization Model Development for Fire Suppression Devices”, M.S. Thesis, University of Maryland-College Park, 2005.
- [16] Wu, D., Guillemin, D., Marshall, A. W., “A Modeling Basis for Predicting the Initial Sprinkler Spray”, *Fire Safety Journal*, Vol. 42, pp. 283-294, 2007.
- [17] Ren, N., “Analysis of the Initial Spray from Canonical Fire Suppression Nozzles”, M.S. Thesis, University of Maryland-College Park, 2007.
- [18] Ren, N., Blum, A., Wu, D., Marshall, A., “Characterizing The Initial Spray from Fire Suppression Devices”, International Mechanical Engineering Congress and Exposition, Chicago, Illinois, Nov. 5-10, 2006.
- [19] Ren, N., Blum, A. F., Zheng, Y., Do, C., and Marshall, A. W., “Quantifying the Initial Spray from Fire Sprinklers”, *Fire Safety Science – Proceedings of the Ninth International Symposium*, IAFSS, Karlsruhe, Deutschland, Accepted, 2008.
- [20] Watson, E. J., “The Radial Spread of a Liquid Jet over a Horizontal Plane”, *Journal of Fluid Mechanics*, Vol. 20, pp. 481-499, 1964.
- [21] Lasheras, J. C., Villermaux, E., Hopfinger, E. J., “Break-up and Atomization of a Round Water Jet by a High-speed Annular Air Jet”, *Journal of Fluid Mechanics*, Vol. 357, pp. 351-379, 1998.
- [22] Lefebvre, A. H., *Atomization and Spray*, First Edition, CRC, 1988.
- [23] Crowe, C.T., Sommerfeld, M., and Tsuji, Y., *Multiphase Flows with Droplets and Particles*, CRC Press, 1998, ISBN 0-8493-9469-4.
- [24] Ibrahim, E. A., and Przekwas, A. J., “Impinging Jets Atomization”, *Physics of Fluids A*, Vol. 3, pp. 2981, 1991.